

NON-INTERACTING BLACK HOLE BINARIES WITH GAIA AND LAMOST

GRZEGORZ WIKTOROWICZ^{1,2}, YOUJUN LU^{1,2}, LUKASZ WYRZYKOWSKI³, HAOTONG ZHANG¹, JIFENG LIU^{1,2,4}, STEPHEN JUSTHAM^{1,2,5}, KRZYSZTOF BELCZYNSKI⁶

¹ National Astronomical Observatories, Chinese Academy of Sciences, Beijing 100101, China

² School of Astronomy and Space Science, University of the Chinese Academy of Sciences, Beijing 100012, China

³ Astronomical Observatory, Warsaw University, Al. Ujazdowskie 4, 00-478 Warsaw, Poland

⁴ WHU-NAOC Joint Center for Astronomy, Wuhan University, Wuhan, China

⁵ Astronomical Institute Anton Pannekoek, University of Amsterdam, P.O. Box 94249, 1090 GE, Amsterdam, The Netherlands

⁶ Nicolaus Copernicus Astronomical Center, Polish Academy of Sciences, Bartycka 18, 00-716 Warsaw, Poland

Draft version January 1, 2021

ABSTRACT

Until recently, black holes (BHs) could be discovered only through accretion from other stars in X-ray binaries, or in merging double compact objects. Improvements in astrometric and spectroscopic measurements have made it possible to detect BHs also in noninteracting BH binaries (nBHs) through a precise analysis of the companion’s motion. In this study, using an updated version of the *StarTrack* binary-star population modeling code and a detailed model of the Milky Way (MW) galaxy we calculate the expected number of detections for Gaia and LAMOST surveys. We develop a formalism to convolve the binary population synthesis output with a realistic stellar density distribution, star-formation history (SFH), and chemical evolution for the MW, which produces a probability distribution function of the predicted compact-binary population over the MW. This avoids the additional statistical uncertainty that is introduced by methods that Monte Carlo sample from binary population synthesis output to produce one potential specific realization of the MW compact-binary distribution, and our method is also comparatively fast to such Monte Carlo realizations. Specifically, we predict $\sim 41\text{--}340$ nBHs to be observed by Gaia, although the numbers may drop to $\sim 10\text{--}70$ if the recent ($\lesssim 100$ Myr) star formation is low ($\sim 1 M_{\odot} \text{ yr}^{-1}$). For LAMOST we predict $\lesssim 14$ detectable nBHs, which is lower partially because its field of view covers just $\sim 6\%$ of the Galaxy.

Subject headings: stars: black holes, gravitational waves, binaries: general, methods: numerical, methods: statistical, astronomical databases: miscellaneous

1. INTRODUCTION

Black holes (BHs), by definition, are very hard to detect electromagnetically¹. Recently, the Event Horizon Telescope collaboration has detected a silhouette of a supermassive BH (Event Horizon Telescope Collaboration et al. 2019) and merging BHs have been detected through gravitational wave emission (Abbott et al. 2016). Some methods like microlensing (e.g. Minniti et al. 2015; Wyrzykowski et al. 2016; Wyrzykowski & Mandel 2019; Wiktorowicz et al. 2019b; Masuda & Hotokezaka 2019), tidal disruption events (e.g. Perets et al. 2016; Kremer et al. 2019), or accretion from dense interstellar medium (e.g. Tsuna et al. 2018) provide a way of detecting free-floating BHs. BHs bound in binaries may be detected through interactions with their companion stars. If the separation is small enough that the companion is able to fill its Roche lobe (RL) during its evolution, stable mass transfer (MT) may occur and the system will become observable as an X-ray binary (e.g. Novikov & Zel’dovich 1973; Wijnands & van der Klis 1998; Zdziarski & Gierliński 2004; Gilfanov 2004; Życki & Niedźwiecki 2005; Maccarone et al. 2005; Fabbiano 2006; Middleton et al. 2012; King & Lasota 2014; Tetarenko et al. 2016), although some systems can be hard to detect owing to low luminosities (e.g. Menou et al. 1999). When the sepa-

ration (a) is larger, the MT through RL overflow (RLOF) cannot occur, but the X-ray emission may be powered by wind accretion. However, the MT through stellar wind is typically small (but see, e.g. Mohamed & Podsiadlowski 2012; Liu et al. 2013; El Mellah et al. 2019), and the emission is in general weaker than from RLOF-fed systems. Nonetheless, even in the absence of interactions, the orbital motion of the visible star detected either astrometrically or spectroscopically may indicate the presence of an invisible companion (e.g. Casares et al. 2014; Giesers et al. 2018; Liu et al. 2019a; Thompson et al. 2019). If, additionally, the mass of the hidden object is estimated to be large ($M \gtrsim 3 M_{\odot}$), then we have a strong claim for a BH, because a regular star of such a mass should be very luminous (e.g. Karpov & Lipunov 2001; Yungelson et al. 2006). Detection of these noninteracting BH binaries (nBHB) in ongoing and future surveys is a promising way of estimating the BH population of our Galaxy.

The Gaia mission of the European Space Agency (Gaia Collaboration et al. 2016b), with its unprecedented astrometric precision and number of observed stars, will provide a perfect database for a variety of statistical studies. Gaia scans the entire sky over the period of 5 yr and delivers multiepoch photometric and astrometric observations of more than a billion stars. Regular subsequent data releases (Gaia Collaboration et al. 2016a, 2018) have provided, among many other products, positional parameters (positions, parallax, and proper motions) for nearly all monitored stars; however, the individual time series

¹ Theoretically, they produce Hawking radiation (Hawking 1974, 1975)

of the astrometric data will be released in the final data release, opening a new vault for scientific exploration. Gaia astrometry was already claimed to be useful in detecting invisible companions (e.g. Gould & Salim 2002; Tomsick & Muterspaugh 2010; Barstow et al. 2014; Igo-shev & Perets 2019). Recently, Gandhi et al. (2020) used astrometric noise in the DR2 data release as a proxy for orbital motion in unresolved binaries identifying viable candidates for in-depth observations.

Kawanaka et al. (2017) and Mashian & Loeb (2017) made a proof-of-concept analytical estimation of the expected number of nBHB systems potentially detectable by Gaia through its 5 yr long mission. Yamaguchi et al. (2018) improved significantly their methodology considering, particularly, an interstellar absorption and obtained prediction of 200–1000 nBHBs discoverable in the Gaia data. The method was further employed by Yalinewich et al. (2018), who added the treatment of natal kicks (NKs; e.g. Herant 1995; Hobbs et al. 2005; Fryer & Kusenko 2006; Fryer & Young 2007; Kuznetsov & Mikheev 2012), the binary fraction, and the simple spatial distribution model, obtaining a prediction of 50–150 nBHBs. Additionally, Shikauchi et al. (2020) found through N -body simulations that ~ 10 nBHBs formed in open clusters may be present in the Gaia data.

All the previous research, however, suffers from a significant drawback, which is the lack of any treatment of binary interactions that may affect the predecessors of nBHBs (Wiktorowicz et al. 2019b, hereafter W19). The first study of these, which included binary interactions through employing the population synthesis (PS) method, was Breivik et al. (2017), who derived an estimate of 3, 800–12, 000 nBHBs, depending on the assumed Gaia astrometric precision. Additionally, their work included an improved Milky Way (MW) model and took into account that we actually observe projected orbits. Recently, Shao & Li (2019) performed a similar calculation using different code and model assumptions and estimated several hundred potential detections for Gaia.

Another way of detecting BH companions in nBHBs is the measurement of radial velocity (RV) variations through spectroscopic observations (e.g. Trimble & Thorne 1969; Giesers et al. 2018; Khokhlov et al. 2018; Makarov & Tokovinin 2019; Thompson et al. 2019). One of the contemporary instruments devoted to spectroscopical observations is LAMOST, which has 4000 fibers and can take spectra of thousands of stars in a single observation. Therefore, it is perhaps the best instrument that can be used to search for spectroscopic binaries by monitoring numerous stars over a long period.

Recently, Gu et al. (2019) used LAMOST DR6 and investigated six red giants (RGs) with detected high ($> 80 \text{ km s}^{-1}$) RV variations. Their results show that on the basis of available data the presence of a BH primary cannot be rejected for all of these stars. The same type of systems was a target of the Zheng et al. (2019) study, which utilized LAMOST data supported by ASAS-SN photometry, but also with no clear detections. Yi et al. (2019) calculated the predicted detection rate of nBHBs by LAMOST. They used a method similar to Mashian & Loeb (2017) and have used simple substitutions to binary formation and stellar evolution process, meanwhile totally ignoring the binary interactions. Their result

TABLE 1
SUMMARY OF MODELS

Model	Difference with Respect to Standard Model
STD	Standard (reference) model: Distribution of initial periods $P(\log P) \propto (\log P)^{-0.55}$ Distribution of initial eccentricities $P(e) \propto e^{-0.42}$ BH/NS NKs are drawn from Maxwellian distribution with $\sigma = 265 \text{ km s}^{-1}$ BH NKs reduced by fallback Moderate slope for high-mass end of the IMF $\Gamma = -2.3$
SS0	Distribution of initial separations $P(\log a) \propto 1$ Distribution of initial eccentricities $P(e) \propto e$
NK _R NK _{BE}	BH NKs are inversely proportional to the BH's mass BH/NS NK proportional to ratio of ejecta mass and remnant mass
flatIMF	Flat slope for high-mass end of the IMF ($\Gamma = -1.9$)
steepIMF	Steep slope for high-mass end of the IMF ($\Gamma = -2.7$)

NOTE. — All main parameters are provided only for the STD model. For other models, only differences in respect to the STD model are given explicitly. Reproduced from Wiktorowicz et al. (2019b).

claimed 50–400 nBHBs potentially observable by LAMOST.

In this work we want to significantly improve previous predictions using publicly available² models of BH populations in different stellar environments (W19). We predict the number of nBHBs present in the M, with a particular attention paid to these that will be observable by Gaia and LAMOST. In Section 2 we describe the utilized database, the model for the MW, and limitations that were imposed on the synthetic results in order to obtain observational predictions. Section 3 is dedicated to the presentation of the results and comparison of different models. In Section 4 we compare our results with previous studies and discuss the problem of interpreting an observation as an nBHB. The summary is provided in Section 5.

2. METHODOLOGY

2.1. Binary evolution models

We use the publicly available database of BHs in different stellar environments (W19). Their calculations were performed with the recent version of the *StarTrack* PS code (Belczynski et al. 2002, 2008, 2020a). We take 18 models from this database: six of their main models (see Table 1): STD, SS0, NK_R, NK_{BE}, flatIMF, and steepIMF, which were calculated for solar metallicity ($Z = Z_{\odot} = 0.02$), and the same models but with different values of metallicity ($Z = 10\% Z_{\odot} = 0.002$, and $Z = 1\% Z_{\odot} = 0.0002$)³. This allowed us to account for the metallicity distribution in the Galaxy for each of the models. From now on, where we talk about a particular model, we talk about three metallicity models combined. Below, we summarize the most important properties of the models (W19, see Tab. 1 and Section 2 for further

² <https://universeathome.pl/universe/bhdb.php>

³ Specifically, models STD, SS0, NK_R, NK_{BE}, flatIMF, steepIMF, lowZ, lowZ_SS0, lowZ_NK_R, lowZ_NK_{BE}, lowZ_flatIMF, lowZ_steepIMF, midZ, midZ_SS0, midZ_NK_R, midZ_NK_{BE}, midZ_flatIMF, midZ_steepIMF.

details).

W19 performed simulations of homogeneous populations of stars with the same initial metallicity and no imposed star formation history (SFH). Their results may be therefore used as "building blocks" for more complicated stellar systems like galaxies, what we do here for the MW. The binaries were evolved in isolation of what is a justified argument for such sparse stellar systems like galactic disks (although see Klencki et al. 2017). We note that interactions between stars and binaries can be important in dense stellar systems like the galactic nuclei, or globular clusters (e.g. Morawski et al. 2018). The interactions between stars in binaries, which were included in the simulations of W19, may in general affect the evolution of an nBHB predecessor. Such interactions include tidal interactions, NKs imparted on the compact object after formation, MT phases, common envelope (CE), etc. All of them, especially NKs, may change the properties of the population significantly and cannot be neglected.

In Table 1 we summarize the models used in the study for the convenience of the reader (the models are discussed thoroughly in W19). The standard model (STD) is the most conservative one. The initial binary parameter distributions of orbital periods and eccentricities follow these observed by Sana et al. (2012), but we have extended them to include mass ratios lower than 0.1 and the full range of primary masses (0.08–150 M_{\odot}). The initial primary masses were drawn from the broken-power-law distribution with power-law index $\Gamma = -1.3, -2.2,$ and -2.3 for mass below 0.5 M_{\odot} , between 0.5 and 1.0 M_{\odot} , and above 1 M_{\odot} , respectively. Mass ratios were drawn from uniform distribution, securing the lower limit for the secondary mass at 0.08 M_{\odot} . The NS and BH NKs are drawn from the Maxwellian distribution with $\sigma = 265 \text{ km s}^{-1}$ (Hobbs et al. 2005). In the case of BHs, we reduce the kicks proportionally to the fallback (i.e. we multiply them by $1 - f_{\text{fb}}$, where f_{fb} is the fraction of mass that falls back onto the compact object).

Other models are variations of the STD model. In the SS0 model the distribution of initial separations is flat in logarithm ($P(\log a) \propto 1$ with $a_{\text{max}} = 10^5 R_{\odot}$), whereas the eccentricities have initially thermal distribution ($P(e) \propto e$). Models NK_R and NK_{BE} introduce new models for NKs. The NK_R model gives kicks inversely proportional to BH mass $v_{\text{kick}} \propto M_{\text{BH}}^{-1}$ (Rodríguez et al. 2016), whereas the NK in the NK_{BE} model is proportional to the ratio of ejecta and remnant mass $v_{\text{kick}} \propto M_{\text{ejecta}}/M_{\text{BH}}$ (Bray & Eldridge 2018). The flatIMF and steepIMF models present variations in the steepness of the initial mass function (IMF) for massive stars ($M_{\text{ZAMS}} > 1 M_{\odot}$) with $\Gamma = -1.9$ and -2.7 , respectively.

2.2. Milky Way model

The detailed structure of the MW and, especially, its past evolution is still not well constrained. The MW galaxy is believed to have a complex structure similar to a barred spiral galaxy. The main components consist of a thin disk and a thick disk, a bulge, and a halo. The observations proved that different components differ not only in the spatial distribution of stars but also in the SFH and chemical composition. Here we model each of the mostly homogeneous components separately in order to obtain a realistic model of the MW and its history.

The usefulness of describing complex stellar systems with small building blocks was already pointed out by Bahcall & Soneira (1981)

In Table 2, we present the model used for the spatial distribution of stars in the Galaxy. We use normalized stellar number density distributions of stars provided by Robin et al. (2003) as a proxy for the spatial distributions of nBHBs. Table 2 also provides metallicities and SFHs (both star formation rates and intervals), which are slightly simplified versions of those in Olejak et al. (2019, hereafter O19). The modification of their metallicity distribution is motivated by the range of models available in W19. O19 based their model on observational data (e.g., Bullock & Johnston 2005; Soubiran & Girard 2005) and cosmological simulations (e.g. Kobayashi & Nakasato 2011) and it treats the chemical evolution in more detail (see also Vos et al. 2020). We note that the SFH in the Galaxy is actually poorly known and may differ by an order of magnitude depending on the observational method used for the constraints (e.g. Chomiuk & Povich 2011).

The duration of the star formation in our model is exactly the same as in O19. The star formation rate in the thin disk we choose to be constant (Mutch et al. 2011, but see Romano et al. 2010) and equal to 4.7 $M_{\odot} \text{ yr}^{-1}$ so that the total mass of the disk (thin and thick) is $5.2 \times 10^{10} M_{\odot}$ (see $5.17 \times 10^{10} M_{\odot}$; Licquia & Newman 2015). As far as the bulge is concerned, we slightly lowered the star formation rate during the constant star formation phase to 4.5 $M_{\odot} \text{ yr}^{-1}$, in order to get the total mass of the bulge equal to 9.1 $\times 10^9 M_{\odot}$ (see Licquia & Newman 2015). Also, we chose the star formation rate in the halo to be higher, so the total stellar mass is $1 \times 10^9 M_{\odot}$ to account for recent measurements using the Gaia data (e.g. Belokurov et al. 2018; Helmi et al. 2018).

The metallicity distribution in the disk is chosen to be constant during the cosmic time in contrast to O19 who provide a relation between the metallicity and the stellar age. We also change the metallicities in MW components to fit models available from W19. Specifically, we choose the thin disk to have solar metallicity $Z = Z_{\odot}$ regardless of the age of stars. The thick-disk metallicity is chosen to be $Z_{\odot}/10$, which is ~ 2 times lower than in O19. For the bulge, we assume the solar metallicity both during the burst and during the following constant star formation. The metallicity in the halo we adopt as constant and equal $Z_{\odot}/100$ through the duration of star formation, which is assumed to have occurred in a single star formation burst $\sim 10 \text{ Gyr}$ ago, which is in agreement with recent estimations made using Gaia data (e.g. Helmi et al. 2018; Matteucci et al. 2019). See O19 and references therein for more details.

We choose to impose an outer limit on the Galaxy at the distance $R_{\text{lim}} = 30 \text{ kpc}$ from its center. It is motivated by observations (e.g. Sesar et al. 2011) which show that at $R_{\text{lim}} \approx 30 \text{ kpc}$ the density gradient becomes very steep. The halo may actually extend to hundreds of kiloparsecs, but the fraction of stellar mass outside of R_{lim} is negligible, and, actually, few stars are found outside of $R = 15 \text{ kpc}$.

Although it was shown that the disk and the halo may exchange mass (e.g. Fox et al. 2019), no MT between the Galactic components is included explicitly in our model.

TABLE 2
MODELS OF THE MILKY WAY COMPONENTS

Component	$M_{\text{tot}} [M_{\odot}]$	SFR [$\frac{M_{\odot}}{\text{yr}}$]	$t_{\text{SF,start}}-t_{\text{SF,end}}$ (Gyr)	Z	$\frac{dN}{dV}$
Thin disk	4.7×10^{10}	4.7	10–0	Z_{\odot}	$\exp(-\frac{(a/5)^2}{2.5}) - \exp(-\frac{(a/3)^2}{2.5}) + \exp(-\sqrt{0.25 + (a/2.53)^2}) - \exp(-\sqrt{0.25 + (a/1.32)^2})$
Thick disk	5×10^9	2.5	11–9	$Z_{\odot}/10$	$\exp(-\frac{R-R_{\odot}}{2.5} \times (1 - \frac{z^2}{0.8}))$
Halo	1×10^9	0.5	12–10	$Z_{\odot}/100$	$\exp(-\frac{R-R_{\odot}}{2.5}) \times 1.32 \times \exp(-\frac{ z }{0.8})$
Bulge	9.1×10^9	2.3 / 0.45	12–10 / 10–0	Z_{\odot}	$(\frac{0.5}{R_{\odot}})^{-2.44}$ if $a \leq 0.5$
					$(\frac{a}{R_{\odot}})^{-2.44}$ if $a > 0.5$
					$\exp(-0.5 \times r_s^2)$ if $R \leq 2.54$
					$\exp(-0.5 \times r_s^2) \times \exp(-2(R - 2.54)^2)$ if $R > 2.54$

NOTE. — The table presents the model MW components used for the presented study. Presented are M_{tot} —total stellar mass of the component; SFR—star formation rate; $t_{\text{SF,start/end}}$ —look-back time of the start and end of star formation episode, which is also the range of ages of the stars in the component; Z —metallicity ($Z_{\odot} = 0.02$ is the solar metallicity); dN/dV —normalized number density of stars (based on Robin et al. 2003); x, y, z - galactocentric position coordinates in kpc (solar position was assumed to be at $x_{\odot}, y_{\odot}, z_{\odot} = 8.3, 0, 0$); $R_{\odot} = 8.3$ is the distance of the Sun from the Galactic center in kpc; $R = \sqrt{x^2 + y^2}$; $a = \sqrt{R^2 + z^2/\epsilon^2}$, where $\epsilon = 0.0551$ for the thin disk and $\epsilon = 0.76$ for the halo; $r_s = \sqrt{[(x/1.59 \text{ kpc})^2 + (y/0.424 \text{ kpc})^2]^2 + (z/0.424 \text{ kpc})^4}$; SFR was assumed to be constant during the star formation phase. The values for SFR and t_{age} were taken from Olejak et al. (2019). For the bulge, there are two star formation episodes

Undetected mass exchange may affect the SFH, but the presented analysis, which depends solely on the rate of star formation, not its sources, is unaffected by this process. Also, mass accretion from intergalactic medium (e.g. Oort 1969) is neglected.

We assume $R_{\odot} = 8.3$ kpc (Gillessen et al. 2009; de Grijs & Bono 2016). The thin-disk mass estimation is very sensitive to the chosen value of R_{\odot} (Bovy & Rix 2013), so we choose a value consistent with Robin et al. (2003). For practical reasons, we assume that the Sun is located at the galactic plane ($z_{\odot} = 0$). The Sun may actually reside slightly above the Galactic plane (e.g. $z_{\odot} \approx 20$ pc; Yoshii 2013), but such a small deviation will not influence our results noticeably. Also, we choose the location of the x-axis and y-axis in the employed Cartesian coordinate system in such a way that $x_{\odot} = 8.3$ kpc and $y_{\odot} = 0$.

For the purpose of this study and to facilitate future research, we have calculated cumulative distributions of stellar mass as a function of distance from the Sun (f_{gal}) with the division on different Galactic components (Figure 1). Precisely,

$$f_{\text{gal,Gaia}}(< D) = \iiint_{\sqrt{(x-x_{\odot})^2 + y^2 + z^2} < D} \frac{dN}{dV}(x, y, z) dx dy dz,$$

$$f_{\text{gal,LAMOST}}(< D) = \iiint_{\substack{\sqrt{(x-x_{\odot})^2 + y^2 + z^2} < D \\ \delta \in [-10^{\circ}, 65^{\circ}] \\ \alpha \in [0^{\circ}, 280^{\circ}]}} \frac{dN}{dV}(x, y, z) dx dy dz,$$
(1)

where dN/dV is the stellar number density defined in Table 2, D is the distance from the Sun, and the integration goes over a sphere centered at the Sun $\vec{r}_{\odot} = (x_{\odot}, y_{\odot}, z_{\odot}) = (8.3 \text{ kpc}, 0, 0)$. We assumed that the edge of the Galaxy is located at $D_{\text{max}} = 30$ kpc from the Galactic center and no stars are present outside of this

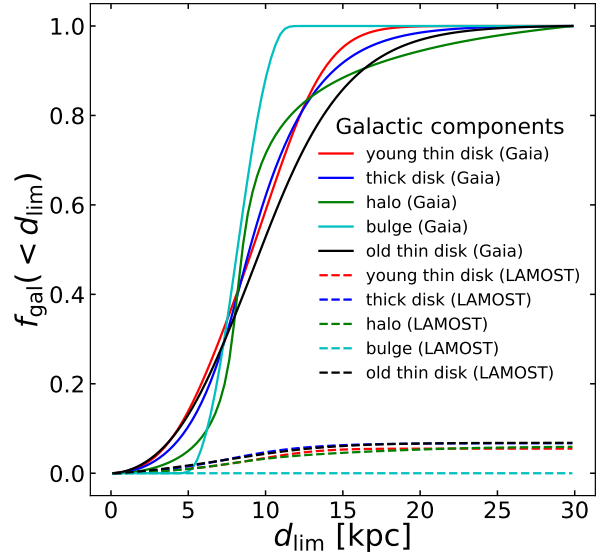


FIG. 1.— Fraction of the MW galaxy component stellar mass (f_{gal}) within the distance D from the Sun in the Gaia (solid lines) and LAMOST (dashed lines). The LAMOST field of view is limited to declinations -10° to 65° and right ascensions 0° – 280° which covers ~ 5 – 7% of the Galaxy. Different lines represent different Galactic components (see Table 2).

radius (see, e.g., Sesar et al. 2011). As LAMOST observes only a fraction of the sky, f_{gal} for LAMOST is always lower than for Gaia $f_{\text{gal,Gaia}}$, which observes the entire sky; LAMOST’s limited field of view (declinations -10° to 65° and right ascensions 0° – 280°), which covers only 5–7% of the Galactic stars depending on the Galactic component (except the bulge, where the fraction is $\sim 0\%$; see Table. 3), must be included in the integration.

TABLE 3
LAMOST FIELD OF VIEW

Component	fraction	
Thin disk	0.055	if $t_{\text{age}} \leq 0.15$ Gyr
	0.068	if $t_{\text{age}} > 0.15$ Gyr
Thick disk	0.067	
Halo	0.059	
Bulge	$\lesssim 10^{-6}$	

NOTE. — The star number fraction of each Galactic component observable by LAMOST. t_{age} is the age of stars in the component. In contrast to Gaia, LAMOST is able to observe only a part of the sky where decl. is $\delta \in [-10^\circ, 65^\circ]$ and right ascension $\alpha \in [0^\circ, 280^\circ]$, which results in $\sim 5\text{--}7\%$ of each Galactic component being in the field of view, except the bulge, which is totally outside of LAMOST’s observational capabilities (a nonzero fraction results only from the lack of any strict size limit imposed on the Bblge while using the density formula [Table 2], but has no effect on the results).

The low f_{gal} for LAMOST results mainly from not having the bulge and its surroundings (Galactic center coordinates: $\delta_{\text{GC}} = -29^\circ$ and $\alpha_{\text{GC}} = 195^\circ$) in its field of view, where the stellar density is the highest. We note that f_{gal} for LAMOST is *not* just a scaled-down f_{gal} for Gaia and, when normalized, has a generally different shape. It comes from the fact that the stellar density changes differently with distance depending on the direction of observation. The exemplary case is the direction toward the Galactic center and in the opposite direction.

2.3. Observational cut

In a widely utilized approach, the observational cuts are obtained by sampling the external parameter (i.e. not inherent to a binary) distributions (e.g. spatial distributions, distribution of orbital orientations) for all the objects in a relevant population and checking whether the objects on which such parameters are imposed are observable, i.e., comply with all the limitations of a chosen instrument (the observable systems compose, so-called, observational cut). Such an approach can potentially lose a significant amount of information about the systems, since only some combinations (randomly chosen from distributions) of systems’ extrinsic parameters are represented in the sample. In most cases these are the systems with the most typical parameters, which is what is wanted; however, some more rare configurations may occur by chance, which may potentially give a high weight to systems that in real situations are very rare, or in the opposite situation, rare (but interesting) systems may not appear in the results at all. To mitigate this problem, typically, many executions of Monte Carlo-based algorithms are necessary in order to obtain a satisfactory precision and get rid of “artifacts.”

Here we present a novel approach to calculate the estimated number of observed sources from PS results that are free from the above problems. The basic idea is to change the stochastic sampling of extrinsic parameter distributions (esp. those relevant to the observational cut) by multidimensional integration of related probability distributions. The method avoids potential information leaks by using all the data concurrently and omits the introduction of additional statistical uncertainties (in contrast to Monte Carlo-based methods). Specifically, instead of drawing the extrinsic properties of systems and

calculating the visibility indicators as Boolean variables, we propose to calculate the visibility as a probability by integrating normalized distributions of extrinsic parameters. For example, in the case of the spatial distribution, the probability corresponds to the fraction of the Galactic stellar mass within a range where the system is observable from the Earth.

The probability corresponding to a particular system is, de facto, equivalent to the expected number of systems in the realistic population that are similar (have the same intrinsic properties as the synthetic system). The sum of expectations calculated for all systems in the synthetic sample obtained from PS simulations gives the expected number of considered systems in the observational results (after multiplication by the scaling factor f_{scale} , see below). The main strength of this approach is that the procedure produces significantly smaller statistical uncertainties, which originate only from the numerical integration and not from the statistical noise. Consequently, it allows us to obtain stronger constraints on theoretical models. As most of the integration can be done in preprocessing by calculating cumulative distributions of extrinsic parameters, the additional computational cost of this method is constant, and for large data sets the method performs similarly or even better than Monte Carlo-based methods, especially if the former introduces several samplings of the synthetic data set. Below we present how this approach can be applied practically to provide estimations for Gaia and LAMOST.

2.3.1. Procedure for Gaia

To ensure that all orbits are complete, we limit the periods to $P_{\text{orb,max}} = 5$ yr. We note that orbital parameters may be obtained even for incomplete orbits when the observed arc covers at least 75% of the orbit (Aitken 1918). Recently, Lucy (2014) reported that, using Bayesian analysis, it is possible to obtain orbital parameters when the orbit coverage is as low as $\sim 40\%$. Such incomplete orbits may potentially increase the number of predicted detections, but they are not analyzed in this study.

The estimated number of systems visible by Gaia can be obtained through the following formula:

$$N_{\text{nBHB,Gaia}} = \sum_{\text{nBHBs}} \int_{\Delta t_{\text{nBHB}}} dt \int_{b_{\text{comp}}}^{a_{\text{comp}}} da_{\text{proj}} P(a_{\text{proj}}) f_w P(d \leq d_{\text{max}}), \quad (2)$$

where the summation goes through all the nBHBs obtained from the PS simulations (W19). Parameters of the binary ($a, e, M_{\text{BH}}, M_{\text{comp}}, Z, L$, etc.) are obtained from the PS results and in general depend on evolutionary time t . Δt_{nBHB} is the time spent by the system as an nBHB. In the general case, the parameters of the system may change during an nBHB phase, and there can be more than one nBHB phase divided by interaction phases like MT or CE. The integral over the evolutionary time (t) includes these binary parameter changes.

The observed orbit is the orbit of the companion whose semi-major axis (a_{comp}) relates to the binary separation (a) as $a_{\text{comp}} = a M_{\text{BH}} / (M_{\text{BH}} + M_{\text{comp}})$, where M_{BH} and M_{comp} are the mass of the BH and its companion, respectively. a_{proj} is the semi-major axis of the projected

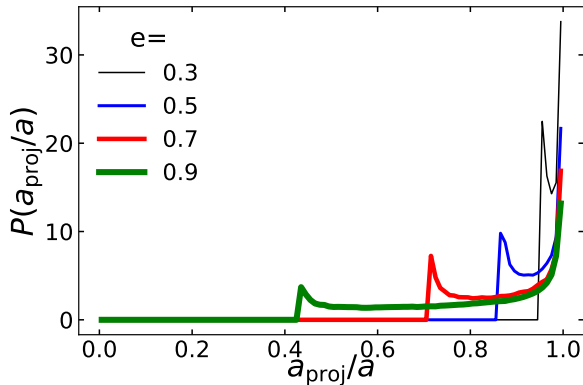


FIG. 2.— Probability distribution for the ratio between the separation of the projected orbit (a_{proj}) and the separation of the original orbit (a) for a few example values of eccentricity (e). All orientations of the original orbit are assumed to be equally probable.

orbit on the plane perpendicular to the line of sight and including the original orbit’s center of mass (we mark this plane as p_{obs}). The plane of the original orbit (p_{orb}) is in general inclined to p_{obs} . To include the projection effect, we calculate the projected orbit on p_{obs} as (see Murray & Dermott 1999)

$$\vec{r}_{\text{obs}} = r \begin{pmatrix} \cos(\omega + f) \\ \sin(\omega + f) \cos(i) \end{pmatrix}, \quad (3)$$

where $r = a(1 - e^2)/(1 + e \cos f)$ describes the original orbit for a parameter f , ω is the position of the periapsis in the p_{orb} plane, and i is the inclination⁴ ($i = 0$ for face-on orbits). The projected orbit has, in general, a different eccentricity and separation than the original one. We calculate a_{proj} as the semi-major axis of the projected orbit.

The semi-minor axis of the companion’s orbit ($b_{\text{comp}} = a_{\text{comp}}\sqrt{1 - e^2}$) and its semi-major axis (a_{comp}) are the minimal/maximal possible values of a_{proj} . The probability distribution of a_{proj} ($P(a_{\text{proj}})$), which depends on the original orbit’s semi-major axis (a) and eccentricity (e), is calculated numerically (see Figure 2). $P(a_{\text{proj}})$ is nonzero only for $a_{\text{proj}} \in [b_{\text{comp}}, a_{\text{comp}}]$. We calculate $P(a_{\text{proj}})$ numerically using Equation 3 and assuming that the positional angle of periapsis is distributed uniformly between 0 and 2π , whereas the inclination has a probability distribution of $P(i) = 0.5 \sin i$.

Weight f_w , which is frequently used for the results of PS simulations, is calculated as

$$f_w = f_{\text{scale}} f_{\text{SFH}} f_{\text{MWC}}(Z), \quad (4)$$

where $f_{\text{scale}} = M_{\text{MW}}/M_{\text{sim}}$ is the scaling factor from the simulated stellar mass M_{sim} to the mass of the MW ($M_{\text{MW}} = 6.08 \times 10^{10} M_{\odot}$; Licquia & Newman 2015). $M_{\text{sim}} = 4.8 \times 10^8 M_{\odot}$ for all the models except steep-IMF and flatIMF, for which it is $1.1 \times 10^9 M_{\odot}$ and $2.4 \times 10^8 M_{\odot}$, respectively. f_{SFH} is a probability that the system will be observed currently, i.e. that it was formed t_{age} years ago. In the case of the model used in this study (Section 2.2), in which the star formation

is constant between $t_{\text{SF,start}}$ and $t_{\text{SF,end}}$ (the values are provided in Table 2 for all MW components), it can be calculated as

$$f_{\text{SFH}} = \frac{\max(0, \min(t_{\text{age}} + dt_{\text{age}}, t_{\text{SF,start}}) - \max(t_{\text{age}}, t_{\text{SF,end}}))}{t_{\text{SF,start}} - t_{\text{SF,end}}}, \quad (5)$$

which is the fraction of the stellar mass formed within $[t_{\text{age}}, t_{\text{age}} + dt_{\text{age}}]$, where dt_{age} is the evolutionary time step from PS (the integral over the nBHB phase duration gives Δt_{nBHB} used in Equation 2). For more general approach to calculating f_{SFH} see Wiktorowicz et al. (2019a, Equation 8).

$f_{\text{MWC}}(Z)$ is a fraction of the MW mass in a Galactic component that has a metallicity Z . According to our MW model, the values of f_{MWC} are equal to $M_{\text{tot}}/M_{\text{MW}}$, where values of M_{tot} are provided in Table 2, for binaries with metallicity Z equal to the metallicity of the MW component (Z in Table 2). f_{MWC} is zero for binaries with different metallicity.

Finally, $P(d < d_{\text{max}})$ is a probability that a randomly located nBHB (according to spatial distributions in Table 2) will have a distance to the observer lower than d_{max} , which is the maximal distance at which the companion is still visible in Gaia, $d_{\text{max}} = \min(d_{\text{astro}}, d_{\text{photo}})$. The limit d_{astro} comes from the fact that the apparent size of the orbit (a_{proj}) must be large enough to enable detection by Gaia. The angular size of the orbit is calculated as $\alpha = a_{\text{proj}}/d = 4.65 \mu\text{as}(a_{\text{proj}}/R_{\odot})(d/\text{kpc})^{-1}$, where d is a distance to the binary. We assume that only systems for which $\alpha > \sigma_G$, where σ_G depend on the object’s apparent luminosity m (Gaia Collaboration et al. 2016b), will be detectable by Gaia. Consequently, d_{astro} comes as a solution to $d_{\text{astro}}\sigma_G(m(d_{\text{astro}}, L)) = a_{\text{proj}}$, where L is the companion’s luminosity and the apparent magnitude m is calculated as

$$m = 5 \log_{10} \left(\left(\frac{d}{\text{kpc}} \right) \left(\frac{L}{L_{\odot}} \right)^{-\frac{1}{2}} \right) + d + 14.83, \quad (6)$$

where we take into account the interstellar extinction as $A(d) = d/\text{kpc}$ (Spitzer 1978, assuming that the Gaia G band is nearly equal to V band). We note that the extinction is expected to saturate at large distances (e.g. Sale et al. 2009) and to be smaller for higher galactic latitudes (e.g. Marshall et al. 2006); however, these effects affect mostly the remote parts of the disk and halo, where only a minor fraction of the Galactic stars are located. Therefore, we use here the simple formula and plan to investigate the effects of extinction in more detail in future work. d_{photo} is the photometric distance, i.e. the distance at which the apparent magnitude of the companion becomes equal to the photometric limit of Gaia ($m_{\text{lim,Gaia}} = 21$) and can be calculated as a solution to $m(d_{\text{photo}}, L) = m_{\text{lim,Gaia}}$.

After we calculate d_{max} , the $P(d < d_{\text{max}})$ can be calculated assuming that the spatial distribution of nBHBs follows the spatial distribution of stars. Then, this probability is equal to the fraction of the Galactic mass within the sphere centered on the Sun and radius $r = d_{\text{max}}$, i.e. $P(d < d_{\text{max}}) = f_{\text{gal}}(d_{\text{max}})$ (Figure 1)

⁴ Here we define inclination as an angle between the normal to orbital plane and the direction toward the observer

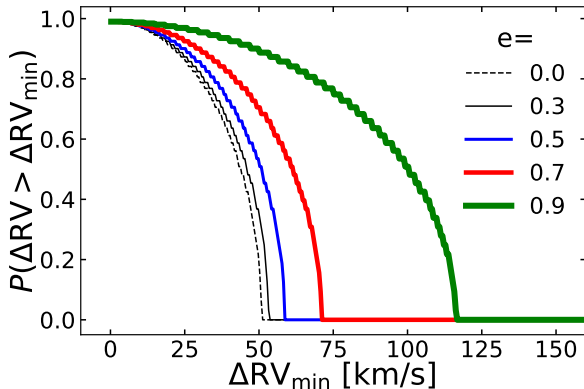


FIG. 3.— Probability distribution of RV variations (ΔRV) being larger than the limiting value (ΔRV_{\min}). Provided values of ΔRV_{\min} are for a reference binary with separation $a = 1 R_{\odot}$ and orbital period $P = 1$ day. For other binaries the scaling should be applied, $\Delta RV = \Delta RV_{\text{obs}}(P/\text{day})(a/R_{\odot})^{-1}$, where ΔRV_{obs} is the observed RV variation for a binary with period P and separation a , in order to use the presented relations. Distributions for a few example values of eccentricity (e) are provided.

2.3.2. Procedure for LAMOST

In the case of LAMOST, in our analysis we have included only stars located in the LAMOST field of view (about $\sim 6\%$ of all stars in the Galaxy; Table 3). As LAMOST is expected to operate longer than Gaia, we chose the maximal orbital period as 10 yr for binaries. As LAMOST is a spectroscopic survey, the procedure is different than for Gaia; however, the general idea stays the same. We calculate the expected number of detections as

$$N_{\text{nBHB,LAMOST}} = \sum_{\text{nBHBs}} \int_{\Delta t_{\text{nBHB}}} dt P(\Delta RV > RV_{\text{err}}) f_w P(d \leq d_{\text{photo}}) f_{\text{visible}}. \quad (7)$$

Similarly to the Gaia procedure (Section 2.3.1), we sum the results for all the binaries in the database, and integration goes over the nBHB phase (Δt_{nBHB}). f_w is calculated in the same way as for Gaia (Equation 4). The other factors are described below.

The change of RV observable by LAMOST has to be higher than the RV error, which is equal to $RV_{\text{err}} = 10 \text{ km s}^{-1}$ for OB stars and lower for fainter stars (Bai et al., in preparation). We calculate a probability that RV of a randomly oriented orbit is higher than this limit as $P(\Delta RV > RV_{\text{err}})$. For any orbital orientation, the RV variation (ΔRV) is calculated as a half of the difference between the highest and lowest RV as observed from the location of the Sun. We assume a random distribution of orbital orientations and calculate this probability distribution numerically (see Figure 3). Only inclined ($i > 0^\circ$) systems can be spectroscopically detectable, but if the orbital velocities are small (e.g. wide circular binaries), the system will not be visible even observed edge-on ($i \approx 90^\circ$). On average, the lower the inclination, the lower is ΔRV , however, for the randomly orientated orbits higher inclinations ($i > 60^\circ$) are preferred to lower ones ($i < 30^\circ$; the probability distribution for the incli-

nation of randomly orientated orbits is $P(i) = 0.5 \sin i$).

$P(d \leq d_{\text{photo}})$ is calculated in the same way as $P(d \leq d_{\text{max}})$ in the Gaia case. The photometric detection limit for LAMOST is lower than for Gaia and equals $m_{\text{lim,LAMOST}} = 16$. We note that as long as the companion is within this magnitude limit, the RV measurements do not depend on distance. Actually, Deng et al. (2012) gave an average V -band limiting magnitude of 18 for LAMOST low-resolution spectrograph, although the LAMOST medium-resolution spectrograph has a smaller V -band limiting magnitude (15 mag; Liu et al. 2019b). However, this limit actually depends on the design of the specific survey. As a parameter study we test also $m_{\text{lim}} = 20$ (see Table 4), which may be reached in future by spectroscopic surveys, like the DESI survey (DESI Collaboration et al. 2016) and PFS survey (Takada et al. 2014). Despite being much deeper, such a survey is expected to increase the detection rates of nBHBs by a factor of only ~ 4 . It results from the fact that the fraction of galaxies observable by LAMOST (f_{gal} ; Figure 1) grows nearly linearly with distance. Equation 6 gives us the following relation between the apparent magnitude limit and the maximum distance to which a particular star is visible:

$$m_2 - m_1 = 5 \log_{10} \frac{d_2}{d_1} + d_2 - d_1. \quad (8)$$

For $\Delta m = 4$ (increase from $m_{\text{lim}} = 16$ to $m_{\text{lim}} = 20$) the distance to which stars are observable increases by a factor of less than 3 if their luminosity is $L \gtrsim L_{\odot}$. For less luminous stars the increase is higher (up to ~ 4), but these stars are still visible only in the vicinity of the Sun ($d \lesssim 3 \text{ kpc}$). As a result, the distance to which the stars are observable grows on average by a factor of ~ 4 (majority of stars observable by LAMOST are low mass, see Section 3). The number of stars observable by LAMOST grows linearly with distance (Figure 1); therefore, the predictions grow also by a factor of ~ 4 (we assume that the spatial distribution of nBHBs follows the spatial distribution of stars). We can also expect that for intermediate values of the limiting apparent magnitude the number of nBHBs observable by LAMOST will change linearly. It is motivated by the fact that in Equation 8 $\Delta d = d_2 - d_1$ dominates over the logarithm, so that $\Delta m \approx \Delta d$. For LAMOST, f_{gal} grows nearly linearly between $d \approx 3 \text{ kpc}$ and 10 kpc (Figure 1); therefore, $N_{\text{nBHB,LAMOST}} \propto f_{\text{gal}} \propto d \propto m$.

f_{visible} is the fraction of a galactic component visible by LAMOST. The values calculated for the LAMOST field of view are provided in Table 3.

3. RESULTS

The main results, i.e. the predicted number of detections, for each tested model are summarized in Table 4. In general, the number of nBHBs detectable by Gaia or LAMOST constitutes only a small fraction ($\lesssim 0.051\%$) of all nBHBs expected to exist currently in the MW. For all models, the fraction is higher for Gaia than for LAMOST by at least one order of magnitude. One of the main reasons is the fact that in the LAMOST field of view there is only a small fraction of the Galaxy ($\lesssim 5\text{--}7$), whereas Gaia observes the entire sky. Additionally, the Gaia sample consists mostly of luminous stars, which are visible from large distances, especially from the vicinity

TABLE 4
PREDICTIONS FOR THE MILKY WAY GALAXY

model	N_{nBHB}	$N_{\text{nBHB,Gaia}}$	$N_{\text{nBHB,LAMOST}}$	$N_{\text{nBHB,LAMOST}^*}$ ($n_{\text{lim}} = 20$)
STD	$1.5 \pm 0.01 \times 10^6$	$1.6 \pm 0.002 \times 10^2$	$1.3 \pm 0.02 \times 10^{-1}$	$2.8 \pm 0.05 \times 10^{-1}$
SS0	$3.2 \pm 0.02 \times 10^6$	$3.4 \pm 0.009 \times 10^2$	$1.3 \pm 0.007 \times 10^1$	$5.0 \pm 0.02 \times 10^1$
NK _R	$1.5 \pm 0.04 \times 10^5$	$7.8 \pm 0.02 \times 10^1$	$1.5 \pm 0.02 \times 10^{-1}$	$3.3 \pm 0.06 \times 10^{-1}$
NK _{BE}	$1.5 \pm 0.04 \times 10^5$	$7.7 \pm 0.02 \times 10^1$	$1.7 \pm 0.02 \times 10^{-1}$	$3.9 \pm 0.05 \times 10^{-1}$
steepIMF	$5.0 \pm 0.05 \times 10^5$	$4.1 \pm 0.006 \times 10^1$	$3.8 \pm 0.09 \times 10^{-2}$	$8.2 \pm 0.1 \times 10^{-2}$
flatIMF	$3.1 \pm 0.03 \times 10^6$	$4.7 \pm 0.004 \times 10^2$	$2.8 \pm 0.03 \times 10^{-1}$	$6.1 \pm 0.09 \times 10^{-1}$

NOTE. — Predictions for the number of nBHBs in the MW (N_{nBHB}) for investigated models. $N_{\text{nBHB,Gaia/LAMOST}}$ are the nBHBs observable by Gaia/LAMOST (see Section 2.3 for the details of the observational cuts). In the case of LAMOST, the limiting apparent magnitude is set to $m_{\text{lim}} = 16$. For comparison, results for the magnitude of a LAMOST-like spectroscopic survey with an apparent magnitude limit of 20 ($N_{\text{nBHB,LAMOST}^*}$) are also provided. The uncertainties were calculated on the basis of 100 bootstrap estimates from a population of $> 10,000$ nBHBs observable by Gaia or LAMOST, which were obtained from PS simulations. For N_{nBHB} Poisson uncertainties are provided. In general, systems observable by Gaia represent a different subpopulation of nBHBs than those observable by LAMOST (see text for details).

of the Galactic bulge. On the other hand, in the LAMOST sample there are more low-mass stars ($\lesssim 2 M_{\odot}$), which obtain higher luminosities ($\gtrsim 200 L_{\odot}$) only after evolving off the main sequence (MS), thus during a short period of their lives. Consequently, nBHB observed by LAMOST reside mostly in the vicinity of the Sun, where the star number density is low in relation to the vicinity of the Galactic center.

The observable fraction by Gaia is the highest for models with higher NKs (NK_R and NK_{BE}). For these models, the total number of nBHBs drops by an order of magnitude, whereas the observed numbers of nBHBs drop by half (Gaia) or two orders of magnitude (LAMOST). The typical companions are responsible for this behavior. In nBHBs, BHs form typically from the primary stars, i.e. the more massive star in each binary on the zero-age MS (ZAMS). As a result of the assumed flat initial mass ratio distribution (W19), lower-/higher-mass secondaries are typically associated with lower-/higher-mass BH progenitors⁵. Only low-mass BH progenitors undergo supernova (SN) explosions with small fallback and, therefore, have significant NKs. Consequently, nBHBs, which might be observable by LAMOST because they have low-mass companions (see Section 3.3) in the STD model, in the NK_R and NK_{BE} models are more frequently disrupted during the BH formation process. We note that some systems may also be excited to wider orbits with periods too large or velocities too small to be detectable by LAMOST. In contrast, the Gaia sample contains mostly nBHBs with massive stars (Section 3.3), which must be accompanied by BHs formed from massive progenitors either with strong fallback (low effective NK) or through direct collapse (no NK).

The steepness of the IMF changes the ratio of high-mass to low-mass stars on the ZAMS. The flatter is the IMF, the more BH progenitors are present in the initial (ZAMS) populations, and their average mass is higher.

⁵ The distribution of primary mass M_a for secondary masses constrained to the range $M_b \in [M_1, M_2]$ can be expressed as a conditional probability $P(A|B)$ where A means the primary mass $M_a = M$ and B means $M_b \in [M_1, M_2]$. The probability can be calculated as $P(A|B) = P(A) * P(B|A)/P(B)$, where $P(A) = \text{IMF}(M)$. $P(B|A)$ is equal to 0 if $M < M_1$, $(M - M_1)/(M - 0.08 M_{\odot})$ if $M_1 < M \leq M_2$, and $(M_2 - M_1)/(M - 0.08 M_{\odot})$ if $M_2 < M$. $P(B) = \int_{M_1}^{M_2} \int_x^{150 M_{\odot}} \text{IMF}(M)/(M - 0.08) dM dx$. $P(A|B)$ drops as $M^{\Gamma-1}$ above M_2 , therefore, if M_2 is small, M_a is also small on average.

The former directly influences the number of nBHBs (N_{nBHB}) and, simultaneously, the numbers of nBHBs observable by both Gaia and LAMOST. In the flatIMF model, in which the IMF is flatter (the IMF exponent $\Gamma = -1.9$) the predicted numbers are higher than in the STD model ($\Gamma = -2.3$), whereas in the steepIMF model ($\Gamma = -2.7$), the numbers are lower (see Table 4). As the tested values of Γ are rather extreme, we may conclude that the steepness of the IMF influences the numbers by a factor of 2–3 in relation to the fiducial model. The higher average mass changes the relative fraction of massive BH progenitors and, consequently, the number of massive secondaries. As a result, the fraction of nBHBs observable by Gaia is higher/lower in the flatIMF/steepIMF model (0.015%/0.008%) than in the reference model (0.011%). The steepness has a smaller effect on the low-mass end of the IMF; therefore, the effect on the fraction observable by LAMOST is negligible (Table 4).

3.1. Formation Routes

Most of the nBHBs in the Galaxy (~ 95 – 96%) were formed without any strong interactions (MT or CE) in the majority of the tested models. The exception are models with increased average NKs (NK_R and NK_{BE}) in which nBHB progenitors are typically disrupted after compact object formation unless some prior interactions harden the system. Consequently, in these models only $\lesssim 5\%$ of systems with no interaction history survive to the nBHB phase. On the other hand, nBHBs in the Gaia and LAMOST samples did undergo an MT or a CE phase (Table 5) prior to the BH formation irrespective of the model. We assumed that the limit on the survey duration is simultaneously a limit for the orbital period of the observable astrometric or spectroscopic binary ($P_{\text{orb}} < 5$ yr for Gaia or 10 yr for LAMOST). We note that binaries with even longer orbital periods can also be potentially detected, but in this study we assumed a conservative limit. These orbital periods translate into a limit on separation of ~ 3000 – $4000 R_{\odot}$. For shorter orbits with separations $\lesssim 1000 R_{\odot}$, BH progenitors, which expand to at least $1000 R_{\odot}$ if evolving as single stars, easily fill their RL and interact with companions through MT or CE. We note that the MT in binaries with mass ratio $q \approx 1$ generally leads to mass ratio reversal and effectively to widening of the orbit. Wider systems with initial separation

TABLE 5
FORMATION ROOTS

Model	Gaia	LAMOST
		All nBHBs
STD	(0.69) MT1(1/2-1) SN1 (0.17) CE1(4-1;7-1) SN1 (0.14) CE1(4-1;7/8-1) SN1 MT2(14-1/2/3/4/5/6)	(0.63) CE1(4-1;7/8-1) SN1 MT2(14-1/2/3/4/5/6) (0.32) CE1(4-1;7-1) SN1
SS0	(0.47) CE1(4-0/1;7-0/1) SN1 (0.34) MT1(1/2-1) SN1 (0.19) CE1(4/5-0/1;7/8-0/1) SN1 MT2(14-0/1/2/3/4/5/6)	(0.87) CE1(4-0/1;7-0/1) SN1 (0.13) CE1(4/5-0/1;7/8-0/1) SN1 MT2(14-0/1/2/3/4/5/6)
NK _R	(0.37) MT1(1/2-1) SN1 (0.33) CE1(4-1;7/8-1) SN1 MT2(14-1/2/3/4/5/6) (0.29) CE1(4-1;7-1) SN1	(0.68) CE1(4-1;7/8-1) SN1 MT2(14-1/2/3/4/5/6) (0.20) CE1(4-1;7-1) SN1 (0.09) SN1
NK _{BE}	(0.37) CE1(4-1;7/8-1) SN1 MT2(14-1/2/3/4/5/6) (0.33) MT1(1/2-1) SN1 (0.30) CE1(4-1;7-1) SN1	(0.79) CE1(4-1;7/8-1) SN1 MT2(14-1/2/3/4/5/6) (0.20) CE1(4-1;7-1) SN1
steepIMF	(0.66) MT1(1/2-1) SN1 (0.17) CE1(4-1;7-1) SN1 (0.16) CE1(4-1;7-1) SN1 MT2(14-1/2/3/4/5/6)	(0.60) CE1(4-1;7-1) SN1 MT2(14-1/2/3/4/5/6) (0.35) CE1(4-1;7-1) SN1
flatIMF	(0.73) MT1(1/2-1) SN1 (0.14) CE1(4-1;7-1) SN1 (0.12) CE1(4-1;7/8-1) SN1 MT2(14-1/2/3/4/5/6)	(0.72) CE1(4-1;7/8-1) SN1 MT2(14-1/2/3/4/5/6) (0.17) CE1(4-1;7-1) SN1
		nBHBs with massive BHs
STD	(0.96) CE1(4-1;7-1) SN1 MT2(14-1/2/3/4) MT2(14-8/9)	(0.95) CE1(4-1;7-1) SN1 MT2(14-1/2/3/4) MT2(14-8/9)
SS0	(0.98) CE1(4-0/1;7-0/1) SN1	(0.98) CE1(4-0/1;7-0/1) SN1
NK _R	(0.91) CE1(4-1;7-1) SN1 MT2(14-1/2/3/4) MT2(14-8/9)	(0.88) CE1(4-1;7-1) SN1 MT2(14-1/2/3/4) MT2(14-8/9) (0.06) CE1(4-1;7-1) SN1 MT2(14-1/2/3/4/5/6)
NK _{BE}	(0.96) CE1(4-1;7-1) SN1 MT2(14-1/2/3/4) MT2(14-8/9)	(0.96) CE1(4-1;7-1) SN1 MT2(14-1/2/3/4) MT2(14-8/9)
steepIMF	(0.96) CE1(4-1;7-1) SN1 MT2(14-1/2/3/4) MT2(14-8/9)	(0.96) CE1(4-1;7-1) SN1 MT2(14-1/2/3/4) MT2(14-8/9)
flatIMF	(0.97) CE1(4-1;7-1) SN1 MT2(14-1/2/3/4) MT2(14-8/9)	(0.96) CE1(4-1;7-1) SN1 MT2(14-1/2/3/4) MT2(14-8/9)
		nBHBs with Massive Companions
STD	(0.99) MT1(1/2-1) SN1	(1.00) MT1(1/2-1) SN1
SS0	(1.00) MT1(1/2-1) SN1	(1.00) MT1(1/2-1) SN1
NK _R	(0.99) MT1(1/2-1) SN1	(0.99) MT1(1/2-1) SN1
NK _{BE}	(0.99) MT1(1/2-1) SN1	(0.99) MT1(1/2-1) SN1
steepIMF	(0.99) MT1(1/2-1) SN1	(1.00) MT1(1/2-1) SN1
flatIMF	(0.99) MT1(1/2-1) SN1	(1.00) MT1(1/2-1) SN1
		Double Compact Objects
STD	(0.59) MT1(1/2-1) SN1 (0.32) CE1(4-1;7-1) SN1 (0.09) CE1(4-1;7-1) SN1 MT2(14-1/2/3)	(0.56) MT1(1/2-1) SN1 (0.21) CE1(4-1;7-1) SN1 (0.14) CE1(4-1;7-1) SN1 MT2(14-2/3)
SS0	(0.68) MT1(1/2-1) SN1 (0.25) CE1(4-1;7-1) SN1 (0.07) CE1(4-1;7-1) SN1 MT2(14-1/2/3)	(0.44) MT1(1/2-1) SN1 (0.24) SN1 MT2(14-2/3/4) (0.13) CE1(4-1;7-1) SN1 (0.10) CE1(4-1;7-1) SN1 MT2(14-1/2/3/4) (0.06) SN1 (0.91) SN1
NK _R	(0.76) CE1(4-1;7-1) SN1 (0.17) CE1(4-1;7-1) SN1 MT2(14-2/3)	(0.50) CE1(4-1;7-1) SN1 MT2(14-1/2/3/4) (0.25) MT1(1/2-1) SN1 (0.24) CE1(4-1;7-1) SN1 (0.64) MT1(1/2-1) SN1 (0.19) CE1(4-1;7-1) SN1 MT2(14-2/3) (0.06) SN1 (0.05) CE1(4-1;7-1) SN1
NK _{BE}	(0.76) CE1(4-1;7-1) SN1 (0.16) CE1(4-1;7-1) SN1 MT2(14-1/2/3) (0.07) MT1(1/2-1) SN1	(0.24) CE1(4-1;7-1) SN1 (0.64) MT1(1/2-1) SN1 (0.19) CE1(4-1;7-1) SN1 MT2(14-2/3) (0.06) SN1 (0.05) CE1(4-1;7-1) SN1
steepIMF	(0.58) MT1(1/2-1) SN1 (0.33) CE1(4-1;7-1) SN1 (0.10) CE1(4-1;7-1) SN1 MT2(14-2/3)	(0.24) CE1(4-1;7-1) SN1 (0.64) MT1(1/2-1) SN1 (0.19) CE1(4-1;7-1) SN1 MT2(14-2/3) (0.06) SN1 (0.05) CE1(4-1;7-1) SN1
flatIMF	(0.65) MT1(1/2-1) SN1 (0.28) CE1(4-1;7-1) SN1 (0.07) CE1(4-1;7-1) SN1 MT2(14-1/2/3/4)	(0.60) MT1(1/2-1) SN1 (0.18) CE1(4-1;7-1) SN1 MT2(14-1/2/3/4) (0.14) CE1(4-1;7-1) SN1

NOTE. — Symbolical representations of the typical evolutionary roots leading to the formation of nBHBs that are predicted to be observed by Gaia and LAMOST. Only main evolutionary phases are presented. The routes for the total samples are presented at the top. Additionally, the typical routes for nBHBs with *massive BHs* ($M_{\text{BH}} > 20 M_{\odot}$), *massive companions* ($M_{\text{comp}} > 30 M_{\odot}$), and nBHBs that are *DCO progenitors* are displayed separately. The numbers in parentheses represent the fraction of nBHBs from a particular subgroup that were formed through this route. The symbols represent the following: SN1—supernova of the primary; MT1/2–MT (primary/secondary is a donor); CE1/2(a1-b1;a2-b2)—common envelope (primary/secondary is a donor; a1/2, primary’s evolutionary type before/after the CE; b1/2, secondary’s evolutionary type before/after the CE). Evolutionary types (numbers inside parentheses) are as follows: 1–MS; 2–Hertzsprung gap; 3–red giant; 4–core helium burning; 5–early asymptotic giant branch; 6–thermal pulsing asymptotic giant branch; 7–helium MS; 8–helium Hertzsprung gap; 9–helium red giant; 13–neutron star; 14–BH.

$a_{\text{ZAMS}} \approx 1000\text{--}4000 R_{\odot}$ and mass ratio $q \approx 1$ (typical for the Gaia sample) also interact, because the RL of the primary is typically $\sim 0.4 \times a \lesssim 1000 R_{\odot}$. In such a case, the CE can be very efficient in decreasing orbital separation. If the MT is stable, usually another phase of MT is necessary after the formation of the BH in order to obtain a binary that can be observed astrometrically by Gaia (or LAMOST). In the LAMOST sample, the companions are typically lighter; therefore, the mass ratio is smaller and the primary’s RL larger ($\lesssim 0.7 \times a \lesssim 3000 R_{\odot}$). In such cases, the primary may not fill the RL during its evolution and the system may stay wide. However, stars on wide orbits have rather slow orbital velocities and, if they have low masses, are visible only in the vicinity of the Sun, which significantly lowers their detection probability by LAMOST, and thus the expected number of detections. As a consequence, the separations of nBHBs in the LAMOST sample are on average smaller than in the Gaia sample. We note that in the LAMOST sample nBHBs are also present with massive companions, which makes it possible for the primary to fill its RL on a wide orbit (see Section 3.3). Systems that have initial orbital periods larger than the assumed detection limits in the absence of interactions tend to expand owing to the loss of orbital angular momentum in stellar wind and so become unobservable by Gaia or LAMOST. Furthermore, such systems, in the lack of interactions, are not expected to become observable by Gaia or LAMOST. For separations higher than $\sim 4000 R_{\odot}$, RLs are generally too large to be filled by typical BH progenitors unless the orbit is significantly eccentric. Then, the RL may be filled in periapsis, where the tidal interactions may circularize the system, and thus significantly lower the initially large separation. Although in the STD model initial eccentricities are typically low, the SS0 model assumes an initial distribution of eccentricities that is skewed toward higher values ($P(e) \propto e$). Therefore, in this model, systems with high initial separations (up to $\sim 10^5 R_{\odot}$) form nBHBs observable by Gaia or LAMOST more frequently than in other tested models, although they have the same initial distribution of masses as the STD model.

Typical systems in a Gaia sample have a BH mass of about $7\text{--}8 M_{\odot}$ and a secondary mass of $35\text{--}50 M_{\odot}$, whereas the typical separation is of the order of $1000\text{--}2000 R_{\odot}$ (Figure 4). Such nBHBs originate from initial binaries with $M_{\text{ZAMS},a} = 45\text{--}55 M_{\odot}$, $M_{\text{ZAMS},b} = 25\text{--}40 M_{\odot}$, and $a_{\text{ZAMS}} = 100\text{--}500 R_{\odot}$ (Figure 5). In the typical scenario (Figure 6), the massive primary fills its RL while expanding on the Hertzsprung gap (HG), or even already on the MS, and transfers mass to the secondary. Meanwhile, the mass ratio reverses and the orbit starts to expand. After the primary forms a BH, the nBHB is observable by Gaia for $1\text{--}2.5$ Myr before the secondary fills its RL owing to evolutionary expansion. The further evolution can be twofold: (1) In the typical case the MT is unstable due to the high mass ratio and results in a CE and, typically, a merger. In other cases, (2) the MT is stable and the donor loses its hydrogen envelope, becoming a helium star. Afterward, the system may be observable as an nBHB with a helium star companion (Figure 9), whose lifetime is, however, much shorter ($\lesssim 0.5$ Myr) than in the case of an nBHB with an MS companion.

In the case of LAMOST, the typical evolution of a progenitor of a detectable nBHB looks different (Figure 7) than in the Gaia case. The progenitors have masses of $M_{\text{ZAMS},a} \approx 30 M_{\odot}$ and $M_{\text{ZAMS},b} \approx 3\text{--}4 M_{\odot}$ separated by $a \approx 4000\text{--}5000 R_{\odot}$ on slightly eccentric orbits $e \lesssim 0.2$ (Figure 5). When the primary fills its RL while being in the CHeB phase, the mass ratio is low ($q < 1/4$), and thus the MT is unstable and a CE phase occurs. The orbital energy of such a wide binary is large enough to eject the envelope of the massive primary and the binary survives as a much closer one ($a \lesssim 100 R_{\odot}$). After the formation of the BH, the system can be detected as an nBHB. Typical BH masses are $7.0\text{--}8.5 M_{\odot}$, whereas companions are typically lighter than $4 M_{\odot}$. The separation is typically between ~ 10 and $100 R_{\odot}$ (Figure 4). After 100 Myr, the secondary evolves off the MS, expands as an HG star, and fills its RL. Then, MT occurs, which widens the system to $a \approx 1000 R_{\odot}$ and results in the loss of the secondary’s hydrogen envelope. Shortly after ($\lesssim 300$ kyr), it becomes a CO white dwarf (WD). On such a wide orbit a WD with its low luminosity would only be detected in a small volume.

3.2. Black holes

The mass distributions of BHs in nBHBs detectable by Gaia and LAMOST are presented in the top-left panel of Figure 4. The majority of these BHs have masses in the range of $5\text{--}15 M_{\odot}$, which is typical for a solar-metallicity environment. Stars with high initial metallicity undergo a strong mass loss in stellar wind, and in the absence of interactions, masses of BHs are limited to about $15 M_{\odot}$. MT from the companion may increase the final BH mass up to $\sim 22 M_{\odot}$ (W19), but configurations allowing for such efficient accretion are very rare in initial populations. Heavier BHs form in lower-metallicity environments. According to our model of the Galaxy, such conditions occur only in the thick disk and halo. These Galactic components constitute only a small fraction ($\sim 10\%$) of the MW’s mass, which is one of the reasons why there are so few expected discoveries of heavy ($\gtrsim 20 M_{\odot}$) BHs in all tested models. In reality, the younger thin disk is expected to have a lower metallicity than assumed in our MW model, which later steadily increases to the current value (see, e.g., Ojajärvi et al. 2019, and references therein). Nonetheless, such a correction is expected to have a minimal effect on the Gaia sample, which is dominated by massive companions, which must have formed recently when the metallicity in the thin disk was already nearly solar. On the other hand, in the LAMOST sample, most of the stars are low mass and may potentially have formed several gigayears ago in a lower-metallicity environment. However, as already said, low-mass secondaries tend to have low-mass primaries that are about to form low-mass BHs, no matter what the metallicity is. Therefore, the effect of metallicity evolution in the thin disk on the distribution of BH masses in nBHBs likely to be observed by Gaia or LAMOST is expected to be small.

BH masses in the LAMOST sample tend to have slightly higher values. Companions in the LAMOST sample are generally lighter than in the Gaia sample; thus, they may potentially originate from older and less metal-rich parts of the Galaxy. Masses of BHs formed in a lower-metallicity environment are expected to be

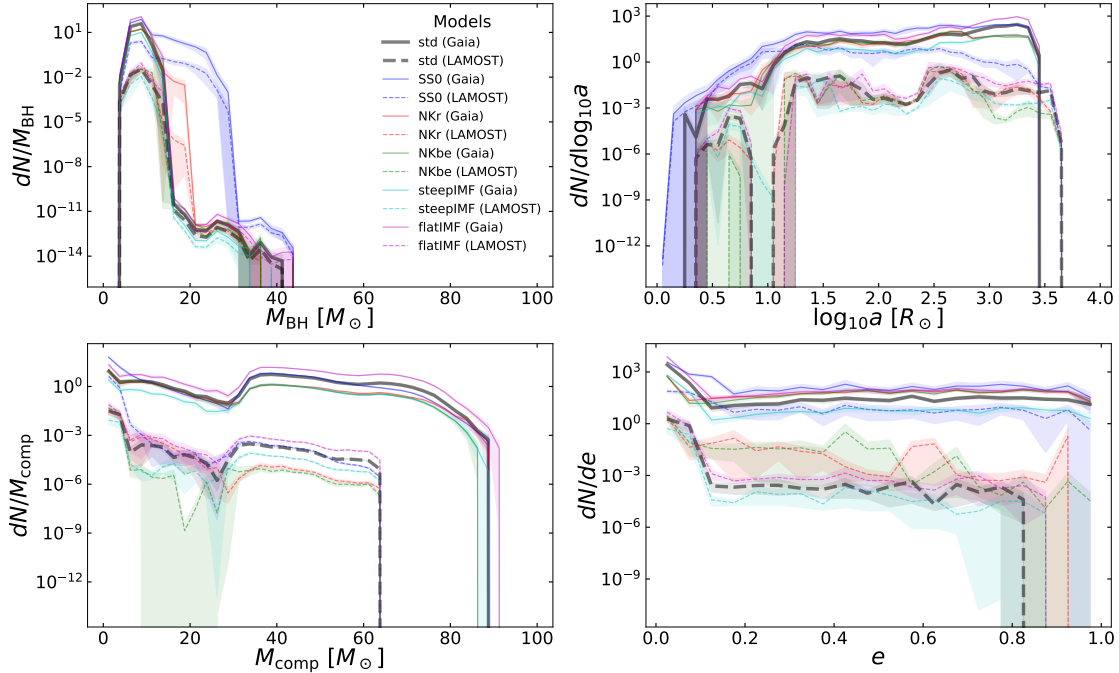


FIG. 4.— Parameter distributions for nBHBs observable by Gaia and LAMOST. A comparison of tested models is provided (see Section 2.1). $M_{\text{BH}/\text{comp}}$ —BH/companion mass; a —separation; e —eccentricity; N —number. Bands represents 95% confidence limits calculated as such $[x_1, x_2]$ such that $x_1 - x_2 = \min\{x'_1 - x'_2 : \sum_{x' \in [x'_1, x'_2]} w_{x'} / \sum_x w_{x'} \geq 0.95\}$ where x' and $w_{x'}$ are data points and their respective weights.

higher on average, therefore pushing the distribution of BH masses toward larger values. However, the fraction of the Galactic stellar mass that has lower metallicity than solar is small; thus, the effect on the typical BH mass is negligible. Except for this feature, the distribution of BH masses observable by LAMOST is similar to that of Gaia, as most of the nBHBs evolve without interactions and originate from the same Galactic component, the thin disk, which composes most ($\sim 77\%$) of the Galactic stellar mass.

The upper BH mass limit in the distributions comes from pair-instability SNe (e.g. Heger & Woosley 2002) and pulsation pair-instability SNe (e.g. Barkat et al. 1967; Woosley 2017). The limit is not strict and depends on modeling (e.g. Farmer et al. 2019; Leung et al. 2019; Mapelli et al. 2020; Renzo et al. 2020). For example, Belczynski et al. (2020a) presented models limiting the maximal BH mass from single-star evolution to values between 45 and 56 M_\odot . Although mass accretion may increase the BH’s mass after its formation, it is by no more than a few M_\odot (W19). Stellar mergers may potentially fill the gap (e.g. Di Carlo et al. 2019). In the absence of strong interactions, pair-instability (pulsation) SNe occur only for stars born with lower ($\lesssim 0.1 Z_\odot$) metallicity, where the helium cores can grow to masses above $\sim 30 M_\odot$ (e.g. Woosley 2017), i.e., in the thick disk and the bulge as far as our MW model is concerned. We note that Liu et al. (2019a) recently discovered a $\sim 70 M_\odot$ BH in the MW. Assuming that this observation is correct (see, e.g., El-Badry & Quataert 2020), such a mas-

sive BH in an nBHB may be in tension with our results. There are three possible explanations: (1) as the authors say, the BH may actually be a very close inner pair or triple in a hierarchical system; (2) the BH may be an outcome of an earlier merger that either happened in a hierarchical system or acquired a companion later on; or (3) the winds assumed in the simulations of W19 were too strong to produce heavy BHs like LB-1 (Belczynski et al. 2019). The first two cases are not subjects of binary PS (see, e.g., Toonen et al. 2017). The third case, i.e. the influence of stellar winds, will be a subject of our future studies.

An interesting behavior is presented by model SS0. Although the majority of nBHBs in the SS0 model have BH masses below $15 M_\odot$, similarly to other models, the fraction of systems with massive BHs ($M_{\text{BH}} > 20 M_\odot$) is much higher ($\sim 1.1\%$ in comparison to $\lesssim 10^{-11}$; Table 6). Model SS0 differs from the reference model only in the initial distributions of separations and eccentricities. Specifically, initial orbits of binaries in the SS0 model are more eccentric, which has significant consequences. Firstly, if the orbit is eccentric, it is much easier for a BH progenitor to fill its RL, which is much smaller when the secondary passes through periastris. Resulting tidal interactions reduce the separation, which can be initially large (up to $10^5 R_\odot$), to observable levels $\lesssim 3000\text{--}4000 R_\odot$. Therefore, the parameter space in initial distributions for nBHB progenitors in the SS0 model also includes wide systems that are not present or very rare

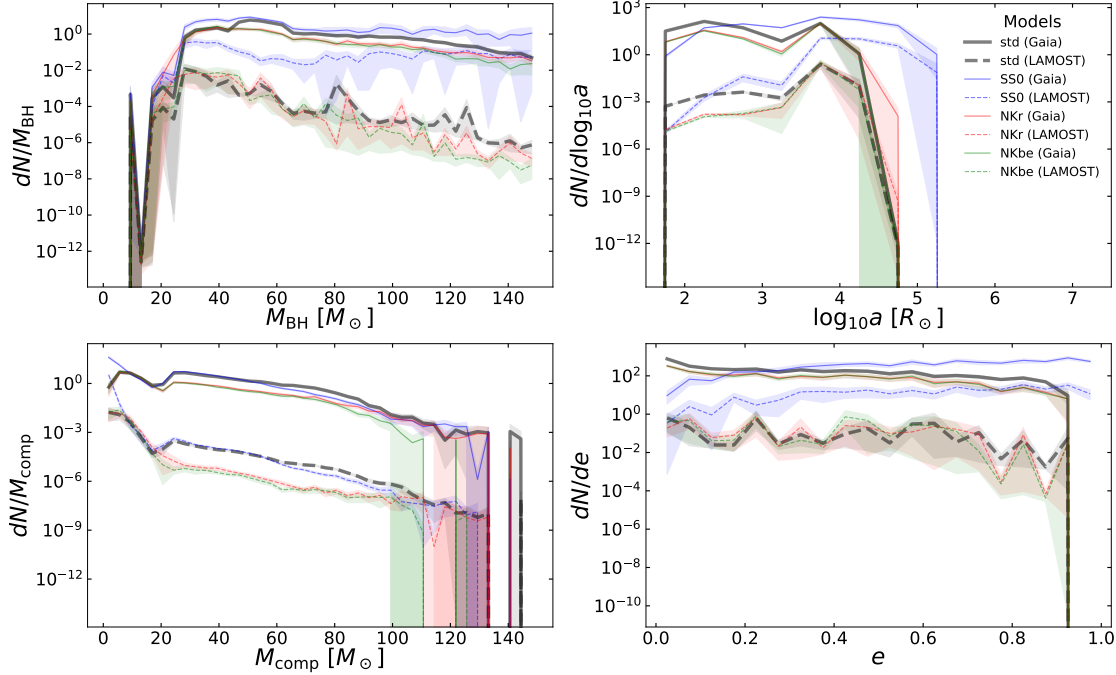


FIG. 5.— Similar to Figure 4, but for initial (ZAMS) populations.

age [Myr]	phase	$M_a[M_\odot]$	$M_b[M_\odot]$
0	MS	53	37
4.2	MT	42 (15)	34 (47)
4.9	SN	7.6	46
6.0	CE	7.7	41.7

Diagram illustrating the evolution of a typical system leading to the formation of an nBHB detectable by Gaia. The system starts as a binary with two main sequence (MS) stars of masses $M_a \approx 53 M_\odot$ and $M_b \approx 37 M_\odot$ and a separation $a \approx 140 R_\odot$. At 4.2 Myr, mass transfer (MT) occurs, with the primary star filling its Roche lobe (RL) and expanding into the Hertzsprung gap (HG). The secondary star is ejected, and the primary star evolves into a helium star (HG) with a mass of 15 M_\odot . At 4.9 Myr, a supernova (SN) occurs, forming a black hole (BH) with a mass of 7.6 M_\odot and a companion star of 46 M_\odot with a separation $a \approx 1,100 R_\odot$. At 6.0 Myr, a common envelope (CE) phase occurs, resulting in a merger of the two stars into a single massive black hole (BH) with a mass of 7.7 M_\odot and a companion star of 41.7 M_\odot with a separation $a \approx 1,200 R_\odot$.

FIG. 6.— Example of a typical system evolution leading to the formation of an nBHB detectable by Gaia. The phases are as follows: ZAMS—zero age MS; MT—mass transfer; SN—supernova, i.e. formation of the BH; CE—common envelope. Stellar evolutionary phases are as follows: MS—main sequence; HG—Hertzsprung gap; BH—black hole. Numbers in parentheses express a change of the parameter during the phase. The binary on the ZAMS is composed of a $\sim 53 M_\odot$ primary and a $\sim 37 M_\odot$ secondary on a relatively short orbit of $140 R_\odot$. After about 4.2 Myr, the primary evolves off the MS and fills its RL while expanding on the HG. The MT commences, which within 1.4 kyr reduces the primary mass to 15 M_\odot . Half of this mass is acquired by the secondary, the rest being rejected from the system. The primary evolves into a helium star and within 700 kyr forms a BH with a small NK. The nBHB forms with an MS companion and a separation of $a \approx 1100 R_\odot$ which lasts for ~ 1.1 Myr. Afterward, the secondary evolves off the MS and fills its RL while expanding on HG. This time the mass ratio is higher, $q \approx 6$, which makes the MT unstable, and the CE occurs. The primary cannot reject the envelope, which results in a merger.

TABLE 6
MASSIVE BHs IN NBHBs

Model	$N_{\text{nBHB,Gaia}}$	$N_{\text{nBHB,LAMOST}}$
STD	1.3×10^{-11} ($7.8 \times 10^{-12}\%$)	4.8×10^{-12} ($3.6 \times 10^{-9}\%$)
SS0	3.8 (1.1%)	1.5×10^{-1} (1.2%)
NK _R	1.5×10^{-11} ($1.9 \times 10^{-11}\%$)	5.9×10^{-12} ($3.9 \times 10^{-9}\%$)
NK _{BE}	1.5×10^{-11} ($2.0 \times 10^{-11}\%$)	5.8×10^{-12} ($3.4 \times 10^{-9}\%$)
steepIMF	2.3×10^{-12} ($5.7 \times 10^{-12}\%$)	8.8×10^{-13} ($2.3 \times 10^{-9}\%$)
flatIMF	3.5×10^{-11} ($7.5 \times 10^{-12}\%$)	1.3×10^{-11} ($4.6 \times 10^{-9}\%$)

NOTE. — Number of nBHBs in Gaia/LAMOST samples that harbor massive BHs ($M_{\text{BH}} > 20 M_\odot$). Numbers in parentheses represent the fractions of the total sample.

in other models. Second, the RLs of BH progenitors in wide but eccentric orbits are small enough to be filled even if the companion is a low-mass star. If the orbit is circular, the primary's RL will be too large for RLOF to occur owing to the small mass ratio. This significantly increases the fraction of nBHBs originating from the old stellar environment, as only low-mass stars can be companions in to such nBHBs. This old lower-metallicity Galactic component may constitute $\sim 10\%$ of the stellar mass in the Galaxy. Consequently, these effects increase the number of nBHBs predicted by the SS0 model to be detected by both Gaia and LAMOST.

In general, massive BHs ($M_{\text{BH}} > 20 M_\odot$) can be found among nBHBs detectable by Gaia and LAMOST in all models, but their fraction among the total population is expected to be, in general, negligibly small (Table 6). These BHs originate from parts of the Galaxy with lower metallicity, i.e. the thick disk and halo. Massive progenitors typically have massive companions; therefore,

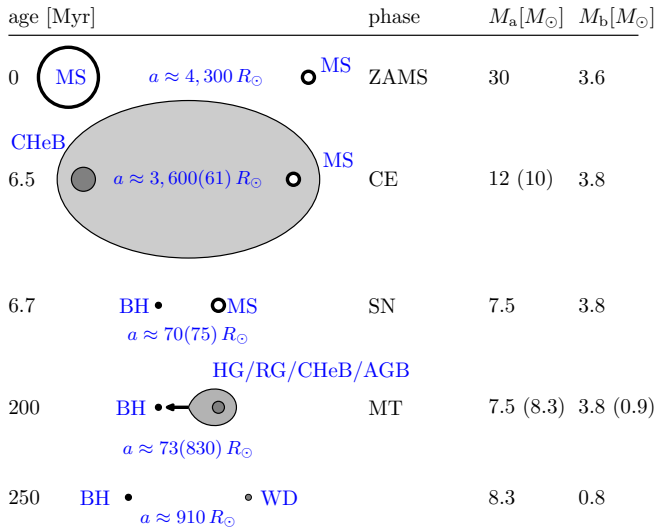


FIG. 7.— Similar to Figure 6, but for typical nBHBs in the LAMOST sample. The additional evolutionary phases (not explained in the caption to Figure 6) are as follows: RG—red giant; CHeB—core helium burning; AGB—asymptotic giant branch; WD—white dwarf. The system begins its evolution as a $30 M_\odot$ and $3.6 M_\odot$ binary on a relatively large orbit of $\sim 4300 R_\odot$. The primary evolves much faster and after 6.5 Myr fills its RL while being on CHeB. The primary is $12 M_\odot$ at that moment, whereas the secondary is $3.8 M_\odot$, therefore, CE commences owing to the high mass ratio. The binary survives, while the separation decreases to $70 R_\odot$. Shortly after, the primary, deprived of its hydrogen envelope, forms a $7.5 M_\odot$ BH with a small NK. An nBHB observable by LAMOST emerges and exists for nearly 200 Myr. Then, the secondary, while expanding on HG, fills its RL and a stable MT starts, which prolongs for ~ 50 Myr. Meanwhile, the secondary evolves and finally becomes a WD, which ends the system evolution. Although being an nBHB, the separation is too high ($a \approx 910 R_\odot$) and the WD too dim to be detectable by LAMOST.

interactions are inevitable if the final orbital period is to be smaller than 5 or 10 yr. In a typical case, the primary fills its RL while expanding during the CHeB phase, which results in a CE. If the system survives the CE, the separation is already significantly smaller. The interactions occur also after the formation of a BH when the secondary expands owing to nuclear evolution and fills its RL. Such a binary might represent an isotropic ultraluminous X-ray sources (ULX) existing in the early MW galaxy (e.g. Wiktorowicz et al. 2019a). However, the thick disk and the halo are old systems; therefore, companions to massive BHs in nBHBs either are low-mass stars ($M_{\text{ZAMS}} \lesssim 1 M_\odot$) or have already evolved into WDs (see Figure 8, bottom left panel). Due to the fact that massive stars had to be accommodated, orbits are relatively large ($a \gtrsim 200 R_\odot$) and circularized owing to interactions (Figure 8, right panels). The number of massive BHs in Gaia and LAMOST samples is small because the birthplaces constrain only a small fraction of the Galaxy ($\sim 10\%$) and the companions are low luminous and therefore observable only in the vicinity of the Sun ($d \lesssim 3$ kpc).

3.3. Companions

Although BH mass distributions for Gaia and LAMOST samples are very similar, the distributions of companion masses show a significant difference. Particularly, the distributions of companions' evolutionary type vary noticeably (Figure 9).

Companions in the Gaia sample are mainly OB stars⁶. Such stars have very short lifetimes ($\lesssim 300$ Myr) and so can be observed only in environments with recent star formation like thin disks or bulges. Such short lifetimes limit the probability of observation, i.e. the probability that the system was born at such a look-back time that it is observable currently (Equation 5). Only a small fraction ($\sim 3\%$) of the thin-disk stellar mass has been formed recently enough to provide OB stars observable currently. On the other hand, among MS stars only OB stars obtain luminosities high enough ($M_{\text{bol}} < -2.7$) to be easily observed by Gaia (apparent magnitude limit of $m_{\text{lim}} \approx 21$) from the vicinity of the Galactic center ($D \approx 8.3$ kpc), where most of the stellar mass is spatially localized ($\gtrsim 60\%$ of the young thin disk is farther away than 7 kpc from the Sun; Figure 1).

A large fraction of detectable companions have high masses ($> 30 M_\odot$; Ziółkowski 1972; Langer 2012). Such stars must have formed quite recently ($\lesssim 10$ Myr) and thus are expected to have rather high metallicities. Therefore, these stars were even heavier on the ZAMS and might have lost a significant fraction of their initial mass in stellar wind. As a consequence, the primaries were also very massive. Such stars expand significantly during their evolution (up to a few $\times 1000 R_\odot$) and fill their RLs, which, due to the limitation put on the P_{orb} , are $\lesssim 1000 R_\odot$. During the resulting MT phase, the primary is typically on the HG or still on its MS (Table 5). The consequence of such a situation is twofold. First, the primary loses its envelope (or most of it) and forms a BH through an SN with an NK (which may be a source of moderate eccentricities), not a direct collapse, which will be otherwise expected. Systems with high eccentricity are assumed to form through an NK during the formation of a BH, because prior to and during a long MT phase or a CE phase eccentric orbits are assumed to circularize rapidly, because of tidal interactions (but for short interactions the circularization may not occur completely; e.g. Eldridge 2009). Second, the secondary becomes rejuvenated and can be observed for longer than a star with similar mass which haven't experienced a mass gain (before going off the MS), which enhances the detection probability. nBHBs with massive companions represent a significant fraction of the Gaia sample ($\sim 22\%$ – 53% ; Table 7) and typically have large separations ($a \gtrsim 100 R_\odot$; Figure 10), as the companion's RL has to be large enough to accommodate it. Both high masses and large separations increase the detection probability by Gaia, but shorter lives ($\lesssim 2$ Myr) partially counteract this effect. Massive stars are expected to be relatively young ($t_{\text{age}} \lesssim 10$ Myr), so they must originate from young Galactic components like the thin disk, which agrees with the typical mass of BHs (7 – $8 M_\odot$, Figure 10), as expected for a solar-metallicity environment (e.g. Belczynski et al. 2010a).

Although OB stars dominate, low-mass stars ($\lesssim 1 M_\odot$) and WDs are also represented in the Gaia sample, especially in nBHBs originating from old Galactic components and containing heavy BHs ($M_{\text{BH}} > 20 M_\odot$). Such companions are dim for most of their life span and thus

⁶ For the purpose of this study, which does not involve spectroscopic analysis, we define an OB star as an MS star with a mass above $M > 2.1 M_\odot$ and effective temperature $T > 11$ kK.

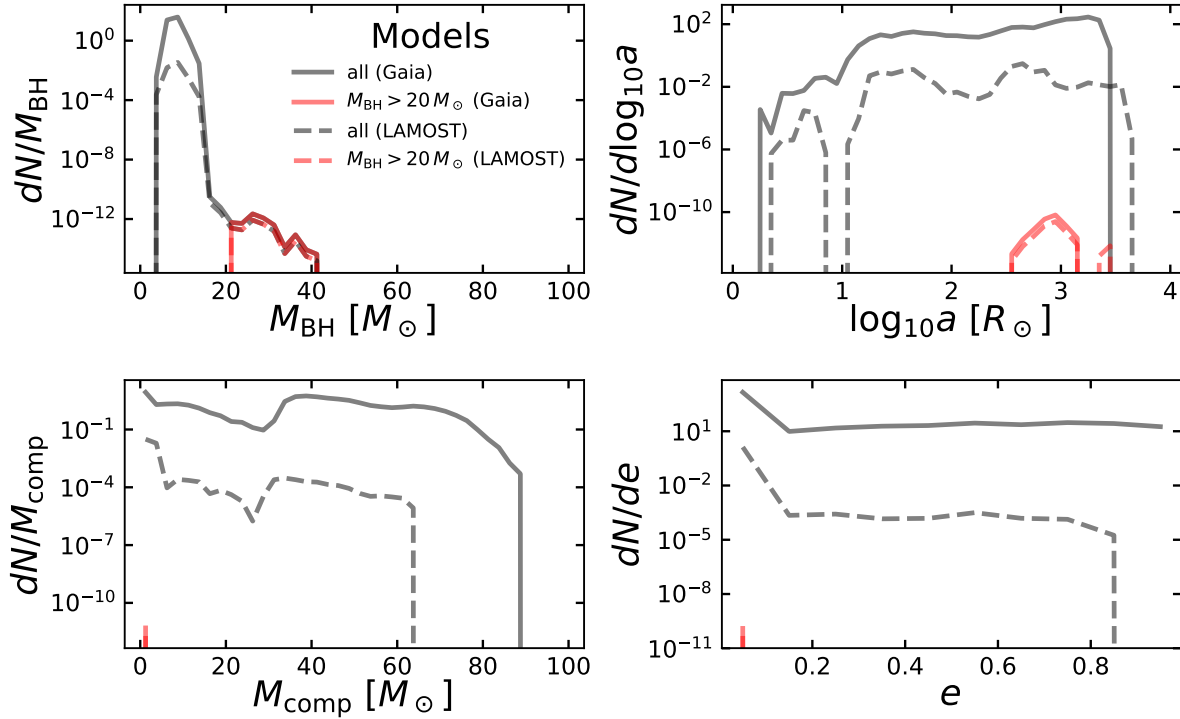


FIG. 8.— Same as Figure 4, but for the STD model only and a subpopulation with massive BHs ($M_{\text{BH}} > 20 M_{\odot}$).

visible only in the vicinity of the Sun ($\lesssim 3$ kpc), where there is only a small fraction of the Galactic stellar mass. Additionally, among companions in nBHB progenitors, low-mass stars and WD progenitors ($M_{\text{ZAMS,b}} \lesssim 8 M_{\odot}$) constitute a smaller fraction of the sample than heavier companions as was already found in W19. On the other hand, the lifetimes of the lighter stars are much longer than OB stars, which gives a higher probability of being observed currently. What is more, they can originate from old Galactic components like thick disks, halos, or bulges, which constitute nearly 1/3 of the Galactic stellar mass.

In spite of being relatively rare in the Gaia sample, nBHBs with low-mass companions constitute the bulk of the LAMOST sample. These are mainly MS stars with masses $\lesssim 4 M_{\odot}$. Such stars have longer life spans than massive OB stars in the Gaia sample and therefore could have been formed in older stellar populations. Some of them have evolved off the MS and became giants in the CHeB phase. Then, their luminosities are on average higher than in the MS phase ($M_{\text{bol}} \sim -0.9$ to -4.4) and so can be observed from higher distances, including the Galactic bulge ($D_{\text{max}} \approx 6.8$ – 9.5 kpc). What is more, surface temperatures of giant stars are significantly smaller in comparison to MS stars owing to their larger radii, which makes the LAMOST RV uncertainty lower (Bai et al., in preparation). On the other hand, a giant star’s lifetime is much shorter than that of its MS predecessor.

Although being strongly biased toward low-mass companions, LAMOST can also detect nBHBs with massive companions (up to $\sim 60 M_{\odot}$). As pointed out above,

TABLE 7
MASSIVE COMPANIONS

Model	$N_{\text{nBHB,Gaia}}$	$N_{\text{nBHB,LAMOST}}$
STD	1.1×10^2 (69%)	4.3×10^{-3} (3.2%)
SS0	1.2×10^2 (34%)	5.3×10^{-3} (0.04%)
NK _R	2.9×10^1 (37%)	1.9×10^{-4} (0.1%)
NK _{BE}	2.6×10^1 (33%)	1.4×10^{-4} (0.08%)
steepIMF	2.7×10^1 (67%)	1.1×10^{-3} (2.8%)
flatIMF	3.4×10^2 (73%)	1.3×10^{-2} (4.4%)

NOTE. — Number of nBHBs in Gaia/LAMOST samples that harbor massive companions ($M_{\text{comp}} > 30 M_{\odot}$). Numbers in parentheses represent the fractions of the total sample.

such binaries have to be wide. Counterintuitively, in the LAMOST sample nBHBs are even larger ($a \gtrsim 1000 R_{\odot}$) than in the Gaia sample. Although larger separations give typically smaller RV variations, if the eccentricities are large ($\gtrsim 0.2$; Figure 10), the RV variations are potentially higher than in similar circular systems because the amplitude of orbital velocity depends on eccentricity as $\Delta v_{\text{orb}} \propto (2 + e^2)/(1 - e^2)$. We note that an eccentric binary spends most of the time in slow phase, which may limit potential detections. On the other hand, massive stars have higher temperatures; thus, LAMOST’s RV variation measurements are less precise (Bai et al., in preparation). In the case of LAMOST, nBHBs harboring companions with masses above $30 M_{\odot}$ are expected in $\lesssim 5\%$ of all the detections (Table 7).

In contrast to those observable by Gaia and LAMOST, the majority of nBHBs in the Galaxy actually have WDs as companions. WD progenitors $M_{\text{ZAMS,b}} \lesssim 8 M_{\odot}$ are

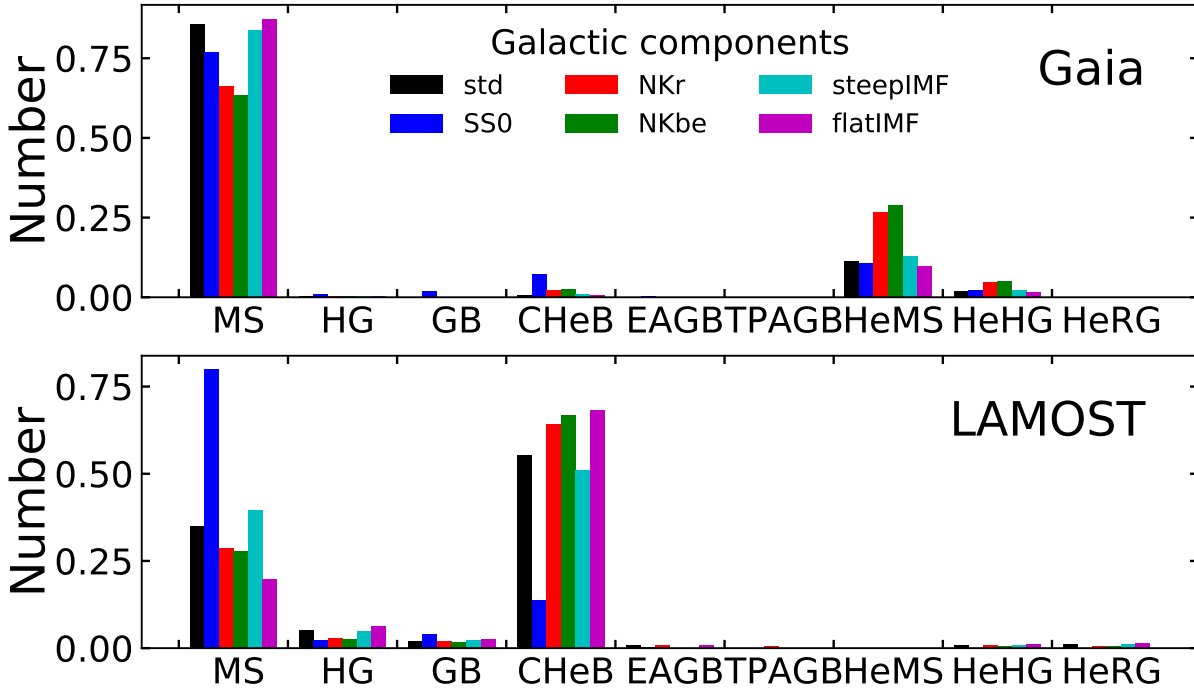


FIG. 9.— Relative fractions of evolutionary types of companions in nBHBs with division on Gaia (top) and LAMOST (bottom) samples. Both populations are dominated by MS companions in any models, but the Gaia sample has typically a significant fraction of helium star companions (HeMS), whereas in LAMOST giant companions (CHEB) are more typical. The symbols represent the following: MS—main sequence; HG—Hertzsprung gap; GB—giant branch; CHEB—core helium burning; EAGB—early asymptotic giant branch; TPAGB—thermally pulsing asymptotic giant branch; HeMS—helium main sequence; HeHG—helium Hertzsprung gap; HeRG—helium red giant.

not a majority on the ZAMS if the mass ratio is assumed to be flat (W19), however, WDs are very long-lived, whereas heavier stars either merge with BH primaries or quickly form a second compact object, which results in binary disruption or formation of a double compact object (double compact objects are undetectable by Gaia and LAMOST and thus are beyond the scope of this paper, although we note that a BH+NS merger may produce radiation in the optical band; e.g., Metzger 2019). For example, if $M_{ZAMS} \gtrsim 1.3 M_{\odot}$, the WD phase is longer than the MS phase for a star born ~ 10 Gyr ago. Nonetheless, WDs compose only a small fraction of the observable sample because their low luminosities allow for detection only in the close vicinity of the Sun ($d \lesssim 25\text{--}1000$ pc; Barstow et al. 2014), i.e. $\lesssim 1\%$ of the total stellar mass of the Galaxy (see Figure 1). Particularly, Torres et al. (2005) and Jiménez-Esteban et al. (2018) estimated that the completeness for WD detection by Gaia can be obtained only up to 100 pc. These estimations agree with the rarity of WDs in nBHBs in the Gaia and LAMOST samples estimated on the basis of our results.

3.4. Separations and eccentricities

The top right and bottom right panels of Figure 4 present distributions of separation and eccentricity, respectively. The Gaia sample is clearly skewed toward higher separations, but the LAMOST sample, although

having on average low separations ($\lesssim 100 R_{\odot}$), has a significant fraction of wide systems that are typically eccentric ($e \gtrsim 0.2$). We note that higher separations not only are rare on the ZAMS but in realistic situations are also prone to disruptions or interactions with field stars (e.g. Klencki et al. 2017).

In the case of Gaia, separations are limited to $\sim 3000 R_{\odot}$ owing to the imposed limit on the orbital period ($P_{\text{orb}} \lesssim 5$ yr) resulting from the mission life span. Wider orbits allow for easier astrometric detection of a companion’s motion from larger distances. For example, with separation equal to $\sim 2000 R_{\odot}$, even the dimmest stars, for which Gaia’s astrometric precision is the worst, are above the astrometric detection limit up to a distance of 15 kpc. However, only the most luminous stars (O type) can be photometrically observed by Gaia from such distances. The preference for circular orbits, arising from tidal circularization occurring typically prior to the BH formation, ensures that the majority of projected orbits, i.e. projections of the orbit on the plane whose normal is parallel to the line of sight, of even highly inclined binaries have separations similarly as large as the original orbits. We note that the semi-major axis of the projected orbit is, in general, not equal to the projection of the semi-major axis of the original orbit. If the orbit is significantly eccentric, the projected orbit may have separation as small as the semi-minor axis of the original orbit. It is, therefore, possible that the separation of the

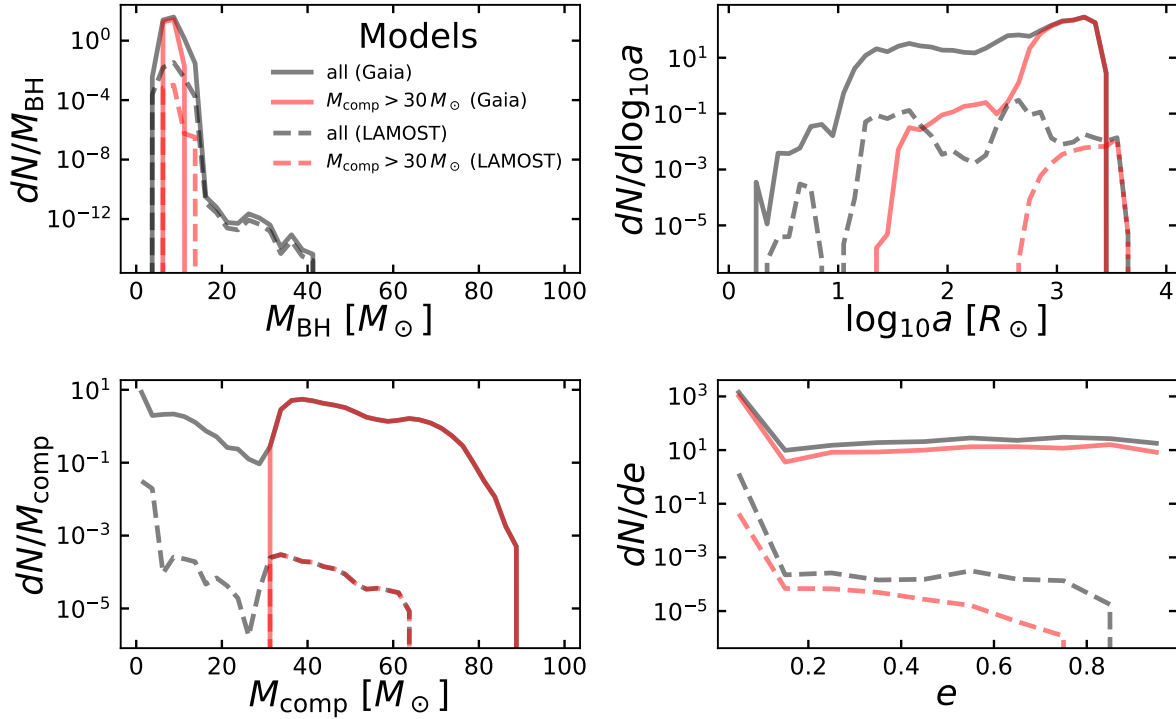


FIG. 10.— Same as Figure 4, but for the STD model only and a subpopulation with massive companions ($M_{\text{comp}} > 30 M_{\odot}$).

projected orbit is below Gaia’s detection limit, although the original orbit is large enough to be detectable. Such situations are included in our procedure (see Section 2.3.1 for further details).

In contrast to Gaia, LAMOST will continue to gather observations for longer-period binaries. Nonetheless, some reasonable limit should still be applied in order to obtain realistic estimates. For the purpose of this study, we assumed $P_{\text{orb}} = 10$ yr as an upper limit for LAMOST. Potentially, even longer-period nBHBs may be observable when the orbit is nearly covered with observations, or the surveys may be extended beyond the assumed ≈ 10 yr. In such a case, the predicted number of nBHBs detectable by LAMOST would increase, but due to the lack of good constraints, we decided to stick to the value of 10 yr. In the case of LAMOST, eccentric binaries may be even easier to detect than circular ones owing to a higher difference in orbital velocity between pericenter and apocenter, but the necessary lack of interactions that may circularize the orbit, or the need for strong NK for a BH, makes their fraction small among detectable nBHBs. Eccentric binaries must also be wide ($\gtrsim 1000 R_{\odot}$); otherwise, the BH progenitor may fill its RL during the periastris passage and the orbit will become circularized by tidal forces or CE evolution.

3.5. Gravitational wave sources

If the BH companion is massive enough to form an NS or a BH, an nBHB may become a double compact object (DCO). The lower mass limit is affected by the binary evolution (MT phases). Even if the companion has a suitable mass, an NK may prevent the formation

TABLE 8
DCO PROGENITORS AMONG NBHBs

Model	$N_{\text{nBHB,Gaia}}$	$N_{\text{nBHB,LAMOST}}$
All		
STD	8.3 (5.1%)	1.2×10^{-3} (0.9%)
SS0	8.5 (2.5%)	2.1×10^{-3} (0.03%)
NK _R	2.5 (3.2%)	2.0×10^{-3} (1.3%)
NK _{BE}	1.6 (2.0%)	8.5×10^{-5} (0.05%)
steepIMF	2.0 (4.8%)	2.9×10^{-4} (0.8%)
flatIMF	23 (4.9%)	3.3×10^{-3} (1.2%)
Merging		
STD	5.3 (3.3%)	7.4×10^{-4} (0.6%)
SS0	5.9 (1.7%)	9.4×10^{-4} (0.01%)
NK _R	0.5 (0.7%)	5.5×10^{-5} (0.04%)
NK _{BE}	0.4 (0.6%)	3.5×10^{-5} (0.02%)
steepIMF	1.3 (3.1%)	2.0×10^{-4} (0.5%)
flatIMF	16 (3.5%)	2.1×10^{-3} (0.7%)

NOTE. — Number of nBHBs in Gaia/LAMOST samples that are progenitors of double compact objects. Numbers in parentheses represent the fractions of the total sample. Both the total population of double compact object progenitors (“all”) and those that have time to merger lower than 10 Gyr (“merging”) are shown.

of a DCO by disrupting the system. Here we present an analysis of DCO progenitors present in both the Gaia and LAMOST samples. For a recent analysis of a broad population of DCOs in the Galaxy (including WDs) see, e.g., Breivik et al. (2020).

Less than $\sim 5.1\%$ of nBHBs detected by Gaia, or less than $\sim 1.7\%$ by LAMOST, are going to form DCOs (Table 8). The rest will either merger or form a BH-WD

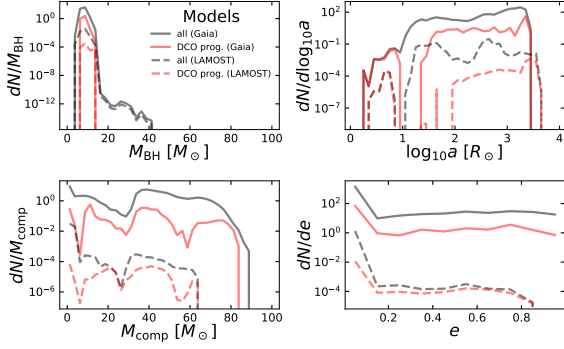


FIG. 11.— The same as Figure 4, but for the STD model only and with separated distributions for DCO progenitors.

system. We note that BH-WD systems are potential gravitational wave sources (e.g. Kremer et al. 2019), but the time to merger is larger than the Hubble time unless the separation is very small ($\lesssim 10 R_\odot$). Nelemans et al. (2001) found through PS study that only three BH-WD mergers per year will be detectable above the noise for LISA in the Galactic disk. Recently, Breivik et al. (2020) argued that none of such systems will be found by this instrument during its 4 yr of operation either in the Galactic disk or in the bulge, adopting a signal-to-noise ratio limit of $S/N > 7$.

The small fraction of DCO progenitors is a direct consequence of the small fraction of massive companions ($\gtrsim 8 M_\odot$, thus DCO progenitors) in nBHBs which are expected to be observed. In the case of Gaia, most of the companion stars are massive enough to form an NS or a BH. However, there are two effects that limit the DCO formation efficiency for these nBHBs. First, most of the companions in these nBHBs are on their MS, which means that their main expansion phase is still before them. Massive stars may fill their RL during the HG and start an MT phase that, due to a typically high mass ratio ($q > 3$), is unstable and leads to a CE phase. A CE phase with HG donors is expected to lead to a merger, because of the lack of a clear core-envelope boundary (Ivanova & Taam 2004), what ends binary evolution. Even if the secondary fills the RL in a later evolutionary phase when its core is well developed, the CE may result in a merger if there is not enough orbital energy to eject its massive envelope. The second factor that limits the number of DCO progenitors for the Gaia sample is the NK. During formation of the second compact object, the kick may disrupt the system, leaving two single stars.

As far as the separation distribution is concerned, the DCO progenitors can be divided into two distinct groups. Those with small separations ($\lesssim 10 R_\odot$) contain helium stars that have lost their hydrogen envelopes as a result of interactions (typically CE) with BHs. These systems are close enough to survive even a strong NK during the formation of an NS where no fallback is expected. However, when the separation is higher ($\gtrsim 10 R_\odot$), the strong NK can easily disrupt the system. DCO progenitors with higher separations are typically MS stars that have not interacted with their primaries after the BH formation. Such separations are large enough to contain a massive ($\gtrsim 8 M_\odot$) compact object progenitor. The fate of these systems is twofold. Either they will inter-

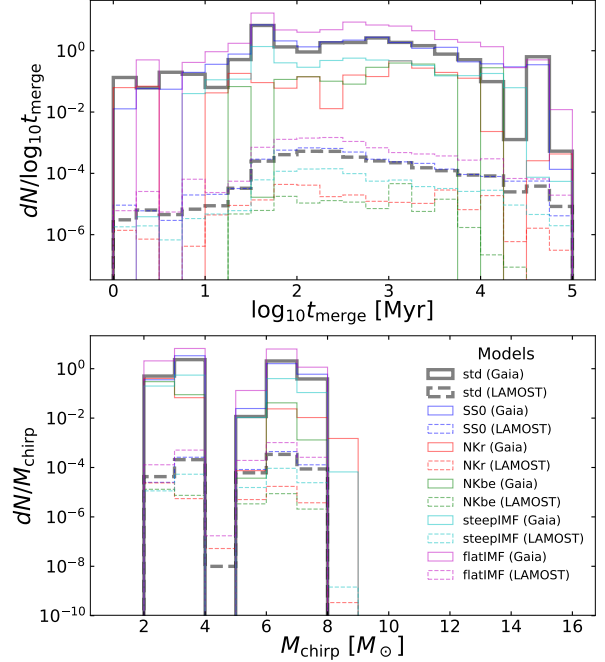


FIG. 12.— Distributions of time to merger (t_{merge}) and chirp mass (M_{chirp}) of DCOs which originate from nBHBs observed by Gaia and LAMOST. The t_{merge} distribution was truncated at 10^5 Myr, which is a much longer time than the age of any Galactic component. Chirp masses are provided only for merging objects. The left peak at $\sim 3 M_\odot$ corresponds to BH+NS systems, whereas that at $\sim 6 M_\odot$ corresponds to BH+BH systems.

act with their primaries as a result of nuclear expansion and lose their hydrogen envelope, effectively joining the systems with low separations and following similar evolution to that described earlier in this paragraph, or their RLs are large enough that the star may evolve without filling them and form a BH through direct collapse or with a small and/or well-directed NK avoiding disruption. The low-separation group typically contains progenitors of BH+NS systems, whereas the more numerous high-separation group contains progenitors of both BH+NS and BH+BH systems.

The formation routes of DCO progenitors are in general similar to the typical routes leading to the formation of nBHBs observable by Gaia and LAMOST (Table 5); thus, many DCOs existing currently in our Galaxy (e.g. Belczynski et al. 2010b) evolved through the nBHB phase. The parameter distributions are similar in shape to those obtained for general population (Figure 11) except for the distribution of separations, as explained above. The lack of DCO progenitors with massive ($> 20 M_\odot$) BHs results from the rarity of nBHBs with massive BHs in the total populations (Figure 4).

The most interesting group among DCO progenitors are those that are going to merge, typically defined as DCOs with time to merger (t_{merge}) lower than about 10 Gyr. Only a small fraction ($\lesssim 5\%$) of nBHBs observable by Gaia or LAMOST are expected to form DCOs, and only part of them will have $t_{\text{merge}} < 10$ Gyr ($\lesssim 70\%$;

see Table 8 and Figure 12). The minimal t_{merge} in our results is 20 kyr, so none of the DCOs that are expected to form from nBHBs that are expected to be observed by Gaia or LAMOST can merge within this time. What is more, massive stars in the Gaia sample are typically still on their MS, whereas evolutionary advanced companions, frequent in the LAMOST sample, are generally low-mass, and thus long-lived, stars. Therefore, the time to DCO formation is generally even longer than t_{merge} . However, there might be some nBHBs that are evolutionary advanced (e.g. nBHBs with helium star companions in the Gaia sample) that can form DCOs in the near ($\lesssim 500$ kyr) future. Such DCOs will emit gravitational waves in the frequency range of $\sim 10^{-4}$ to 10^{-3} Hz with lifetimes of a million years and can be detected by LISA (Babak et al. 2017), Taiji (Ruan et al. 2019), or Tianqin (Wang et al. 2019).

4. DISCUSSION

4.1. Comparison with previous studies

Breivik et al. (2017) was the first to apply detailed PS modeling to study the detectability of nBHBs by Gaia. They used COSMIC, an updated BSE code (Hurley et al. 2002), assuming a primary-mass-dependent binary fraction (van Haften et al. 2013). They included only the thin and thick disks, the former with a total stellar mass of $2.15 \times 10^{10} M_{\odot}$ and constant star formation throughout the past 10 Gyr, and the latter with $2.6 \times 10^9 M_{\odot}$ and burst-like star formation that occurred 10 Gyr ago (Robin et al. 2003). The distribution of stars was adopted after Yu & Jeffery (2015). Using these assumptions, Breivik et al. (2017) obtained a prediction of $(3.8\text{--}12) \times 10^3$ detections during Gaia’s 5 yr life span. Our model SS0 is the one that is the most similar to their assumptions. We obtain an order of magnitude fewer nBHBs (~ 340) in our calculations than their lower limit. The main reason why they obtain much more predicted nBHBs is the lack of any treatment of interstellar extinction included in their analysis, which significantly decreases the volume from which low-mass stars (the majority in their sample) can be observed. Especially, extinction makes it impossible to detect low-mass stars from the vicinity of the Galactic bulge. Other significant differences between their and our analysis, which does not necessarily increase the predicted number of nBHBs, include the lower total stellar mass ($\sim 2.4 \times 10^{10} M_{\odot}$), a continuous relation between the binary fraction and primary mass ($0.5 + 0.25 \log m$), and a lower limit for initial orbital periods of 0.5 days.

Shao & Li (2019) also recently estimated the number of nBHBs observable by Gaia. They performed a study of BHBs with normal-star companions (which they define as a star on the MS or at the (super)giant stage). Similarly to Breivik et al. (2017), they used the binary PS code BSE to simulate the Galactic population of BHBs. In their results, the pre-SN primaries are always helium stars that are assumed to have a probability of 0.6 to become a BH if their mass is larger than $5 M_{\odot}$. The assumed total stellar mass in the Galaxy is $3 \times 10^{10} M_{\odot}$, which is roughly half of the stellar mass assumed in our Galaxy model, and with a constant SFH. Although Shao & Li (2019) included only binaries with initial periods $P_{\text{orb}} < 10 \times 10^3$ days, in contrast to Breivik et al. (2017),

they included interstellar extinction to make the estimate more realistic. They predicted that the population of nBHBs with MS or giant companions observable by Gaia is $\sim 262\text{--}974$ depending on the model. This number is comparable to our model SS0, which is most similar to theirs as far as initial populations are considered. We note that, although their total stellar mass is only about half of what we use in our analysis, they allowed for stable MT for mass ratios as high as ~ 6 , assumed that all stars are in binaries, and in one model (B) allowed for a formation of BHs from stars with initial masses as low as $\sim 15 M_{\odot}$. All these assumptions increase the number of expected nBHBs.

For LAMOST we predict only $\lesssim 14$ detectable nBHBs, which is so low partially because its field of view covers just $\sim 6\%$ of the Galaxy. Our study is the first for this instrument that takes into account binary evolution. Yi et al. (2019) performed a simplified analytical calculation modeled after Mashian & Loeb (2017), and obtain a prediction of $\sim 50\text{--}400$ nBHBs depending on the survey strategy. This number is significantly higher than our most promising estimations (the SS0 model, with 14 expected detections). The difference stems from the fact that their modeling lacks any treatment of interactions between binary components (like RLOF or CE), which, as we show in this study, are prevalent among progenitors of nBHBs in the predicted LAMOST sample. On the other hand, they limited themselves to MS companions only and predicted that they are mostly low-mass stars on close orbits ($P_{\text{orb}} \approx 0.2\text{--}2$ days). The masses in general agree with our prediction, but our periods are typically higher. We note that their choice of uniform distribution of inclinations is biased toward face-on orbits compared to random orbital orientations, which increases their expected number of nBHBs detectable by LAMOST.

4.2. nBHB candidates

Although Gaia and LAMOST are excellent instruments to search for nBHBs, the majority of the systems ($> 99\%$) remain undetectable for them (Figure 13). Up to date, no nBHBs have been detected through astrometry. In fact, only Gaia, with its unprecedented astrometric measurement accuracy, is able to provide a reasonable detection possibility, so we need to wait until the binary astrometric motion is going to be included in the forthcoming Gaia Data Releases or when the raw Gaia observations are available for in-depth study.

Despite many spectroscopic surveys (e.g. Trimble & Thorne 1969; Casares et al. 2014; Gu et al. 2019; Makarov & Tokovinin 2019; Zheng et al. 2019), only a few strong candidates were identified. We note that all these candidates for nBHBs were specifically chosen for detailed analysis because of their luminous companions (RG with $m_V = 12.9$ or B-type stars with $m_V = 11$ and 11.5) and high RV variations ($44 \text{ km s}^{-1} \leq K \leq 53 \text{ km s}^{-1}$). LAMOST is capable of detecting nBHBs with much smaller RV variations ($\lesssim 10 \text{ km s}^{-1}$) and potentially fainter companions ($m_{\text{lim}} \geq 16$).

Khokhlov et al. (2018) analyzed a high RV variation ($K \approx 52 \text{ km s}^{-1}$) binary AS 386 with a B-type star and an invisible companion. The mass function provided a minimal mass for the latter as $1.9 M_{\odot}$. The position of

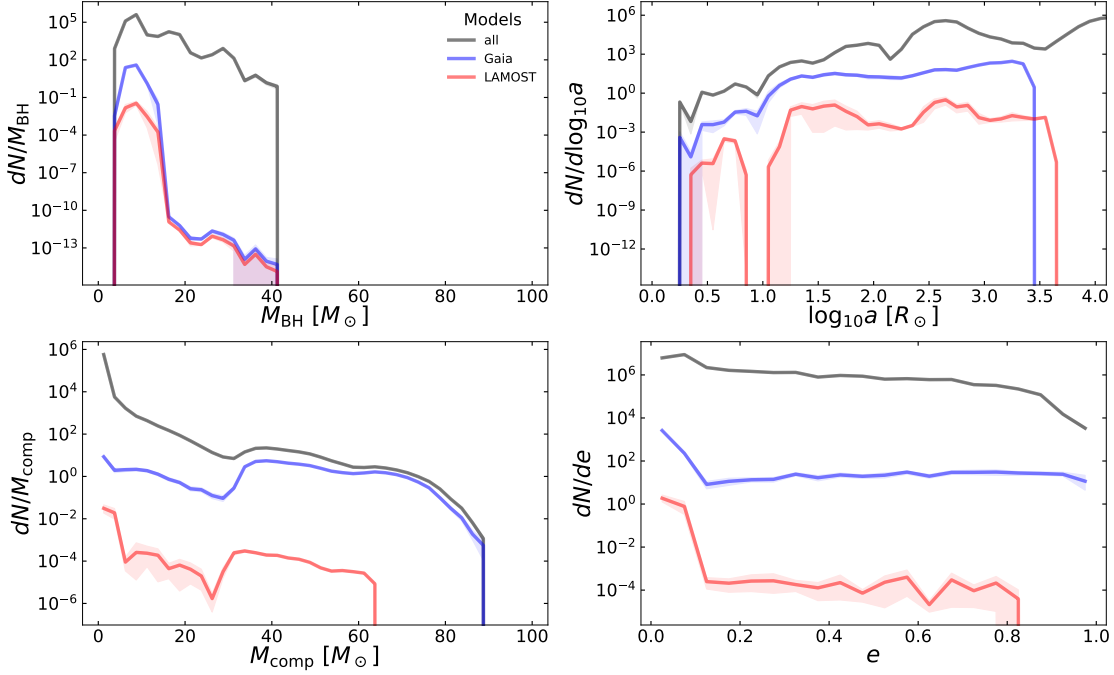


FIG. 13.— Similar to Figure 4, but comparing the entire population of nBHBs (all) with the Gaia and LAMOST samples. Only the STD model is shown for visibility reasons.

the B-type star on HRD suggests a mass of $7 \pm 1 M_{\odot}$. This estimate, compared with the mass function, gives a minimal mass of the invisible companion of $7.3 M_{\odot}$ which makes it a plausible BH candidate. Although the evolution of the B star was probably affected by binary interactions (actually the Doppler tomography showed a presence of dust scattered around the B star, which supports this supposition), as it is typical for sources in the LAMOST sample, so the actual mass may be different. Nonetheless, the presence of a BH in this system cannot be rejected.

Another nBHB candidate was detected by Thompson et al. (2019), who analyzed a 2MASS J05215658+435922 RG star with strong RV variations ($K \approx 44 \text{ km s}^{-1}$) and obtained a mass function of $0.77 M_{\odot}$. Although the orbit is relatively wide ($P_{\text{orb}} = 83$ days), the authors assumed (motivated by low eccentricity $e \approx 0.005$ and similarity of orbital and photometric periods) that the giant’s rotation is synchronized with its orbital motion and were able to assess its radius and imply a mass of the invisible companion of $\sim 3.3 M_{\odot}$.

Recently, Liu et al. (2019a) claimed the discovery of a BH accompanied by a $\sim 8.2 M_{\odot}$ B-type MS star. Interpreting apparent motion of an H α emission line as associated with the BH further leads to a BH mass of $\sim 70 M_{\odot}$. Belczynski et al. (2020b) showed that such massive BHs may be produced through isolated evolution avoiding pair-instability SNe, when the stellar evolution is fine-tuned and for extreme mass-loss assumptions. However, in this study we adopted more conservative evolutionary physics, which could not reproduce such an object. Nonetheless, parameters of the visible

companion were revised by many further studies (e.g. Eldridge et al. 2019; Simón-Díaz et al. 2020; El-Badry & Quataert 2020), and especially Irrgang et al. (2020) suggested that the companion may be actually a low-mass ($1.1 \pm 0.5 M_{\odot}$) stripped star, which is mimicking a B-type MS star. Together with the updated estimation of the binary mass ratio ($\sim 5.1 \pm 0.8$; Liu et al. 2020), the BH mass is lowered to $\sim 4\text{--}36 M_{\odot}$. Yungelson et al. (2020) performed a PS study based on Irrgang et al. finding that such systems can exist in the Galaxy in significant numbers. However, they have not included observability for any instrument in their calculations. We note also that recently Shenar et al. (2020) showed that by disentangling the spectra it can be claimed that the binary actually harbors no degenerate components. This discord motivated us to briefly analyze what is the probability of detecting nBHBs with B-type companions in the Gaia and LAMOST samples aiming at reproducing the LB-1, but retaining a significant parameter freedom. Specifically, we analyzed the presence of nBHBs with hot companions ($10 \text{ kK} < T_{\text{eff}} < 14 \text{ kK}$) and orbital periods of 80 ± 10 days in our Gaia and LAMOST samples. We note that hot stars have significant RV errors in LAMOST observations, which can hinder detection. Such binaries must have gone through interactions like CE or MT, because the orbit is too small ($a \approx 300 R_{\odot}$) to accommodate the BH progenitor, and if the companion is indeed a low-mass star, it can obtain such high temperatures only if their envelopes were stripped off through RLOF. The interaction phase is supported by the detection of surface molecule anomalies that may originate from mass stripping revealing processed material. The

expected number of such binaries is 0.18 in the Gaia sample and 2% of the LAMOST sample for the STD model. Such systems have B-type MS stars, which went through a CE phase, reducing the initial separation of $\sim 5000 R_\odot$ to just $\sim 20 R_\odot$. When the system is ~ 100 Myr old and consists of a $\sim 7 M_\odot$ BH and a young $\sim 4\text{--}5 M_\odot$ B-type MS star, it becomes observable by both Gaia and LAMOST. These numbers are much smaller than obtained by Safarzadeh et al. (2019), who calculated $\sim 60,000$ LB-1-like systems on the basis of the Liu et al. (2019a) observation, and $\lesssim 4000$ on the basis of their analysis. The discrepancy originates from many simplifying assumptions adopted by Safarzadeh et al. (2019), like equal lifetimes of $> 8 M_\odot$ stars, constant SFH, no super-Eddington MT rates, no extinction, etc., and considering only one evolutionary path leading through a ULX phase (we show that nBHBs can form without an XRB (let alone ULX) phase; see Table 5).

To close this subsection, we note here that the predicted number of nBHBs that can be detected by surveys such as Gaia or LAMOST are model dependent. Different models may result in very different numbers, which again suggests that searching for nBHBs using astrometry or RV surveys may put strong constraints on the evolutionary models, their initial conditions, and the structure of the Galaxy.

4.3. Milky Way Model Influence

The spatial distribution of stars in the Galaxy is still very uncertain. In general, it is much harder to estimate global parameters like color or mass for the MW than for other galaxies, because we cannot make an unbiased observation “from inside.” Here we compare the model utilized in this study with other available models in order to estimate the influence the MW model has on our results. Figure 14 presents a comparison between the models for the thin and thick disk, as most of the other studies concentrated on these two components only.

Mashian & Loeb (2017) and Yi et al. (2019) utilized the double exponential model of Jurić et al. (2008) in which $dN/dV \propto \exp(-R/L - Z/H)$, where R , Z are cylindrical galactocentric coordinates and L , H are constants. Figure 14 shows that this model gives $f_{\text{gal}}(d_{\text{lim}})$ very different from other models and, especially, shows a much higher concentration of stars near the Galactic center.

Breivik et al. (2017) employed the model of Yu & Jeffery (2015). This model assumes an exponential relation for the distance from the Galactic center (R) but uses hyperbolic secant for the distance from the Galactic plane (z). As a result, the f_{gal} relation is very similar to the one that we employed in this work, and we expect no significant differences in our results if the model of Yu & Jeffery (2015) was applied for the thin and thick disks.

Another important factor that is not well constrained for the Galaxy is its SFH. Here we assumed that the star formation rate was constant during the start formation periods for all Galactic components, as shown in Table 2. However, such an approach may significantly overestimate the recent star formation in the Galaxy. According to our model, the recent star formation in the thin disk is $4.7 M_\odot \text{ yr}^{-1}$. However, Robitaille & Whitney (2010) estimated a much lower value of $0.68 - 1.45 M_\odot \text{ yr}^{-1}$. Also, Mutch et al. (2011) suggested that the MW is in

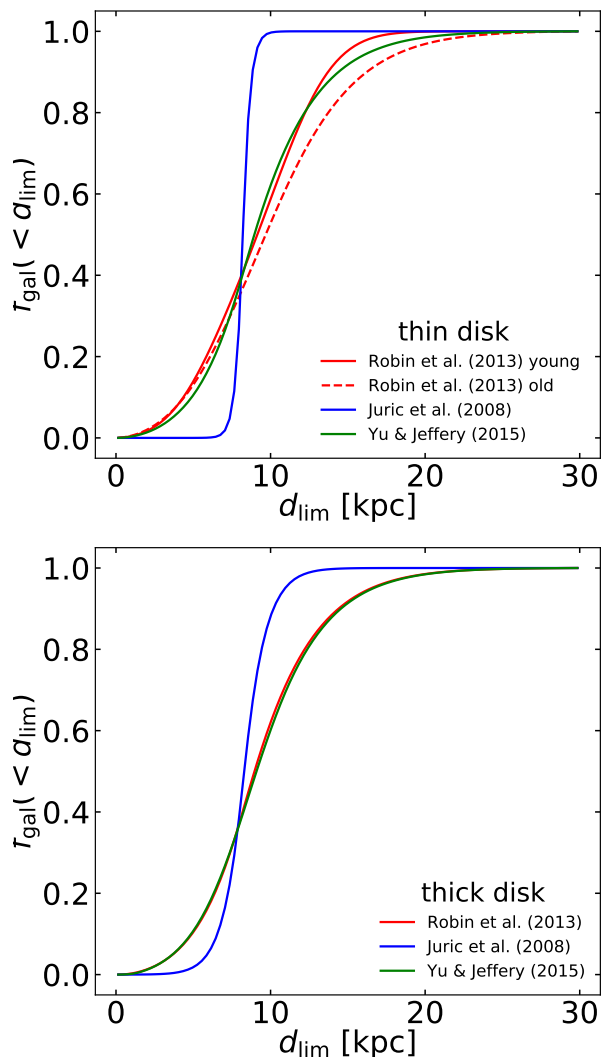


FIG. 14.— Same as Figure 1, but different models of stellar distributions are compared and only thin (top) and thick (bottom) disks are presented.

the state of ceasing star formation and becoming a red spiral galaxy, which suggests a lower recent star formation than average. The lower value of recent star formation will decrease the fraction of massive stars that are present in current stellar populations owing to their short lifetimes. As a consequence, our prediction for the Gaia sample, which consists mostly of nBHBs with massive companions, would decrease by a factor equal roughly to the recent star formation divided by the star formation assumed in this study ($\text{SF}_{\text{recent}}/4.7 M_\odot \text{ yr}^{-1}$). If the recent star formation is indeed $\lesssim 1 M_\odot$, it would mean that the expected number of detections should be lower by a factor of $\gtrsim 4\text{--}5$ compared to the values estimated in this study (Table 4).

What is more, the metallicity and its dependence on location and Galactic age are not known precisely for the MW. The metallicity significantly influences the evolution of stars, especially the mass loss in stellar wind and radial expansion (e.g. Belczynski et al. 2007, 2010b, see also Vos et al. 2020), which plays a crucial role on the final BH mass in an nBHB. Better constraints can significantly alter theoretical predictions.

In this paper we have assumed that the spatial distribution of nBHBs follows the distribution of stars. However, in realistic situations, nBHBs can have different distributions owing to NKs that can change not only binary parameters but also the center-of-mass velocity. Compact binaries ($a \lesssim 10 R_\odot$) can obtain velocities as high as $\sim 300 \text{ km s}^{-1}$ while remaining bound. Therefore, the distribution of compact nBHBs can be much more extended (dynamically hotter) than the distribution of stars. These binaries are not easily detectable by Gaia owing to their smaller sizes, whereas LAMOST has worse accuracy for hotter stars (the result of interaction). Nevertheless, compact nBHBs with large center-of-mass velocities are expected to be rather rare. Wider pairs with slow orbital motions, which are a majority of both the predicted LAMOST and Gaia samples, are prone to disruption if the compact object formation is associated with a significant NK. Binaries that survive the process would acquire only small additional velocities, which means that they will in general follow the distribution of stars as assumed in this work. We note that wide nBHBs are likely to interact with other stars even in the Galactic field (Binney & Tremaine 2008; Klencki et al. 2017), which can lead to disruptions or increase in eccentricity that effectively leads to shortening of the orbital period.

In Figure 15 we present 2D histograms of center-of-mass velocities and orbital periods. The majority ($> 80\%$) of systems have small ($< 20 \text{ km s}^{-1}$) velocities, and only systems with periods less than 100 days obtain significant ($\gtrsim 250 \text{ km s}^{-1}$) velocities. The same relation is observed in the Gaia and LAMOST samples. In addition, we show the distribution of eccentricities in relation to center-of-mass velocities to support the statement that high-velocity systems ($\gtrsim 150 \text{ km s}^{-1}$), which are not wide ($< 700 R_\odot$), quickly circularize ($e \approx 0$), whereas wide systems ($> 1000 R_\odot$) can be eccentric (up to $e \approx 1$).

4.4. Detection probability

Although about 100 nBHBs are predicted to be observed by Gaia during its 5yr long mission, not all of these systems may be recognized as such, due to projection effects. For example, a projected eccentric binary may have a semi-major axis (a_{proj}) smaller than the semi-major axis of the original orbit. It may not only make the astrometric motion of the nBHB unobservable by Gaia, as included in our study, but also hinder the posterior analysis, which is necessary in order to obtain the invisible object's mass.

Provided that the orbital orientation and companion's mass can be inferred from the observations, the hidden object's mass can be calculated from the equation (see

also Andrews et al. 2019):

$$\frac{M_{\text{prim}}^3}{(M_{\text{comp}} + M_{\text{prim}})^2} = \frac{4\pi^2}{GP_{\text{orb}}^2} a_{\text{comp}}^3, \quad (9)$$

where G is the gravitational constant and M_{prim} is the mass of a hidden primary (a BH candidate in our case). Gaia will observe every object on average ~ 75 times, which may provide enough data to constrain the orbital orientation. Otherwise, a_{proj} gives only a lower limit for a_{comp} . Nonetheless, nBHBs observable by Gaia are expected to be nearly circular in most cases, because the tidal interactions during the MT phase preceding the BH formation should circularize even very eccentric orbits, unless the NK was very strong and the orbit is wide. Therefore, as a first approximation we may assume $a_{\text{comp}} \approx a_{\text{proj}}$ for nBHB candidates. Andrews et al. (2019) calculated that, for a companion mass of $10 M_\odot$, nBHBs with a BH of mass $10 M_\odot$ should be detectable at least to a distance of 1 kpc. We find that heavier companions are expected to form a bulk of the Gaia sample and they are observable mostly from the vicinity of the Galactic bulge, which goes beyond their tested distance range.

The other significant problem is the mass of the visible star. In many cases it can be estimated by fitting its spectra to those calculated for single stars, e.g. from PARSEC tracks or single-star PS. We note that not only are such fits typically not very precise, but also the evolution of a star in a binary system can be affected by interactions with the companion. Actually, for nBHB progenitors such interactions are expected to be typical (Table 5). Fortunately, in most cases the MT occurs when the companion is still on its MS. For MS stars, the MT results in rejuvenation of the accretor, because it has enough time to adapt to the increase of its mass and continue its evolution similarly to a single star of accordingly higher mass.

In general, or when the orbital orientation and companion mass have not been derived from the observations, we can estimate the absolute lower limit on the mass of the invisible companion as

$$M_{\text{prim}} > M_{\text{prim,min}} = \frac{4\pi^2}{GP_{\text{orb}}^2} a_{\text{proj}}^3. \quad (10)$$

If $M_{\text{prim,min}}$ is higher than $2.5\text{--}3.5 M_\odot$ (theoretical upper limits for the NS mass) and, simultaneously, the distance to the system is lower than the distance at which a ZAMS star of mass $M_{\text{prim,min}}$ will have apparent magnitude equal to Gaia's limiting magnitude of 21 mag (stars generally tend to increase their luminosity during their evolution), the system contains a plausible BH candidate.

We note that $P_{\text{orb}} < 5 \text{ yr}$ is a limit imposed by the mission duration, not by any physical constraints. Even binaries with longer orbital periods can be detected without their orbit being fully covered by observations, and their parameters will be constrained (Lucy 2014; Docobo et al. 2018). The ability to detect longer orbits may significantly increase the detection rate of nBHBs by Gaia.

The bolometric correction for red supergiants (RSGs; $T_{\text{eff}} \lesssim 4000 \text{ K}$) can be significant (Jordi et al. 2010). However, RSGs constrain only a small fraction of the Gaia sample. First of all, the RSG phase is very short

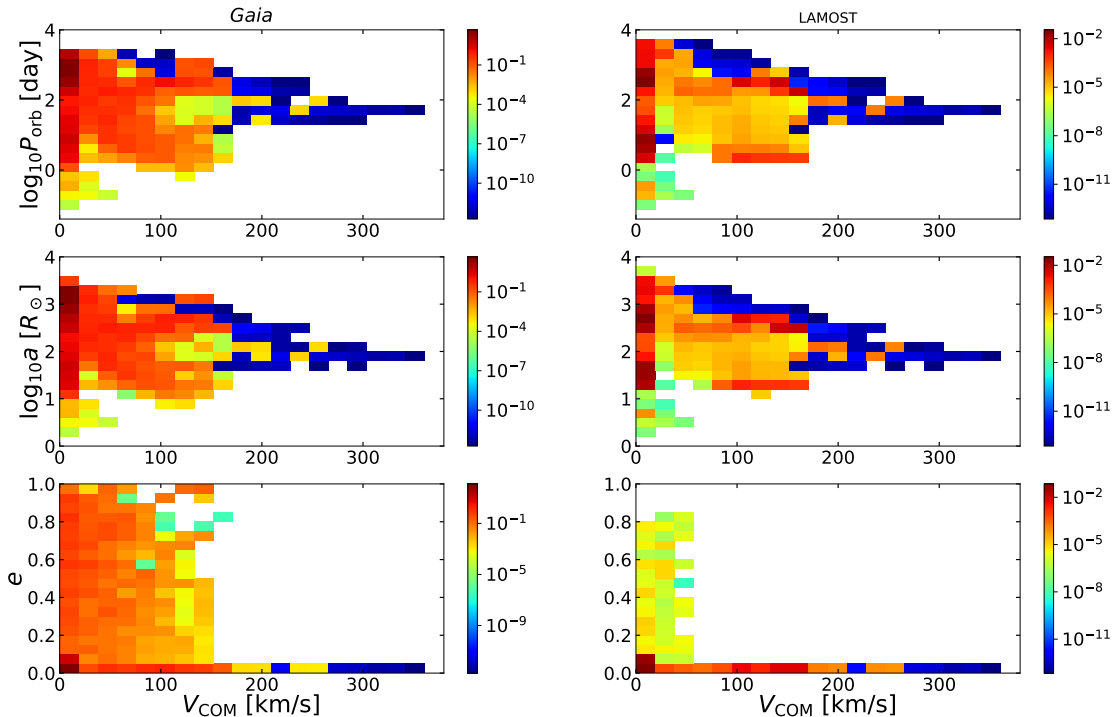


FIG. 15.— 2D histograms of orbital period (P_{orb}) vs. center-of-mass velocity (V_{COM} ; top panels), separation (a) vs. V_{COM} (middle panels), and eccentricity (e) vs. V_{COM} (bottom panels). Results are presented for the Gaia (left panels) and the LAMOST (right panels) samples and the STD model.

in comparison to the MS or WD phases, and solar-metallicity massive stars ($> 40 M_{\odot}$) never expand significantly enough to become SGs owing to significant mass loss. Second, RSG progenitors reach radii of hundreds to thousands of R_{\odot} during their evolution. For high-metallicity stars this occurs by the time the star finishes CHeB and is able to reach high central temperatures necessary for large luminosities (e.g. Wiktorowicz et al. 2019b; Klencki et al. 2020). Additionally, RLOF can remove the outer layers of the stars, raising their effective temperatures. On the other hand, recent simulations (e.g. Laplace et al. 2020) show that the hydrogen envelope may not be fully removed, and the star’s remaining envelope can still expand significantly. To sum up, if the bolometric correction is applied to our results this should not influence significantly the predicted Gaia sample, although we agree that the values we provide should be considered as an upper limit.

Interpreting the LAMOST spectroscopic observations suffers from a similar problem to that of Gaia’s astrometric measurements. The observed RV variations depend on the inclination,

$$K = 50.6 \text{ km s}^{-1} \sin i (a_{\text{comp}}/R_{\odot})(P_{\text{orb}}/\text{day})^{-1}(1-e^2)^{-0.5}. \quad (11)$$

So RV variations from any nBHB visible face-on (inclination $i \approx 0$) will be undetectable, and a mass function calculated from the orbital period and observed RV variations gives only the lower limit for the invisible star’s mass. Additional measurements that allow estimating

the orbital orientation (in the case of LAMOST, only inclination is needed) and the visible star mass are necessary to constrain the invisible object mass. If this is not possible, we are left only with a lower limit coming from the mass function, which allows us to indicate BH candidates using a similar argument as for Gaia (see Equation 10 and the related text), but with the limiting magnitude appropriate for LAMOST ($m_{\text{lim}} = 16$ for the current survey).

In our analysis, we assumed that LAMOST will be able to observe all binaries that are within detection limits (which is the LAMOST sample). However, the number of fibers limits the number of sources that are observed each night, and the number of measurements for a single source is limited. For the current low-resolution survey, the majority of objects are being observed only three times during the same night (cadence of 40–120 minutes), which limits the periods for which RV variations can be detected to $\lesssim 1$ day. Such binaries constitute only a small fraction of the predicted observable LAMOST sample ($a \lesssim 10 R_{\odot}$; see Figure 4, top right panel). The situation can change for the upcoming medium-resolution survey, in which the majority of objects are going to be observed ~ 60 times during a more than 5 yr long observational campaign. Nevertheless, detected RV variations, unless a RV curve can be fitted, can give only lower limits for the intrinsic values of $K = v_{\text{rot}} \sin i$. Therefore, some observable binaries, which are included in the LAMOST sample, may remain undetected owing to rare data coverage. Our evolutionary models, supported by statistical

analysis, find that typical spectroscopic binaries in the LAMOST sample have large separations (and thus large orbital periods, $P_{\text{orb}} \gtrsim 1$ yr; Figure 4). Therefore, regular observations, even if sparse, can prove more efficient for nBHB detection than one-night short-cadence ones. On the basis of our results we can deduce that, if we focus on finding nBHBs and can make only a few observations of one object, a recurrent observations every ~ 1 yr that can detect RV variations for typical nBHBs in the LAMOST sample are a more promising way to detect these sources, which can be realized in forthcoming surveys.

5. SUMMARY

Using the recently published database of model predictions for BHs in different stellar environments (W19), we have constructed a population of nBHBs in the Galaxy using realistic models of the MW’s SFH, chemical evolution, and spatial distributions of stars in different Galactic components (thin and thick disks, halo, and bulge). We applied observational constraints to theoretical evolutionary models in order to calculate the detection rates and properties of nBHBs detectable by Gaia and LAMOST. In such a way we can use observations to constrain the theory. To account for uncertainties in stellar and binary evolution, we analyzed a range of realistic models that provide a better insight into the importance of evolutionary processes on the predictions. To give a broader picture, we discussed how future missions can improve our detection rates of nBHBs.

Specifically, we estimated the total number of BHs in nBHBs present in the Galaxy today as 1.5×10^5 – 3.2×10^6 depending on the evolutionary model employed. However, only a small fraction ($\lesssim 0.05\%$) of these nBHBs can be detected by spectroscopic or astrometric observations of companion stars. We predict that Gaia is able to detect ~ 41 – 340 nBHBs within 5 yr, whereas LAMOST is expected to detect less than 14 nBHBs in a span of 10 yr. The significantly lower detection rate for LAMOST comes mainly from the fact that its field of view encompasses only $\sim 6\%$ of the Galaxy’s stars.

If the possibility of detecting incomplete orbits is taken into account (e.g. Lucy 2014), the numbers may be significantly larger, as many nBHBs are predicted to have orbits wider than 5–10 yr. On the other hand, the poorly constrained SFH, especially recently, significantly affects the estimates. For example, if the recent star formation is as low as $\sim 1 M_{\odot} \text{yr}^{-1}$ (e.g. Robitaille & Whitney 2010), the estimated numbers of nBHB detections for Gaia will drop to ~ 10 – 70 .

Although the typical predicted masses of BHs in nBHBs are similar for both instruments (~ 7 – $8 M_{\odot}$), typical companion masses differ significantly. In the predicted Gaia sample, massive OB stars with masses above $30 M_{\odot}$ dominate, whereas for LAMOST these are mostly low-mass ($\lesssim 4 M_{\odot}$) MS stars. We note that the separations in nBHBs observable by Gaia are expected to

be much larger (~ 1000 – $2000 R_{\odot}$) than those by LAMOST (~ 10 – $1000 R_{\odot}$), mainly due to the different requirements for the detection.

These predictions depend on evolutionary models encapsulated in PS results and models of the Galaxy, both of which can introduce significant errors that are hard to estimate. However, the method we have developed is flexible enough to include future advancements in stellar and binary evolution and the MW composition and history.

We show how important are the treatments of binary interactions, SFH, metallicity, and spatial distribution of stars for the predictions of observational properties of nBHBs. The majority of Galactic stars are located in the vicinity of the bulge ($D \approx 8$ kpc), and therefore observable only if their luminosities are higher than $\sim 400 L_{\odot}$. These stars can be very young as a part of the thin disk and typically have \sim solar metallicity. Less luminous stars are potentially detectable only in the vicinity of the Sun, where the stellar number density is much smaller. Stars of low metallicity are typically old and can be observed mainly in thick disks and halos, where only a small fraction ($\sim 10\%$) of Galactic stars are located. Consequently, inclusion of realistic Galactic properties can significantly change the estimates in comparison to simplified models, especially when old or massive stars are involved. In our work we used recent estimates for these properties and adopted a novel method to include them in population studies. Future detections of nBHBs by Gaia, LAMOST, and other surveys may put strong constraints on binary star evolution and PS models.

We thank Gijs Nelemans for a helpful suggestion. We are thankful to thousands of volunteers who took part in the *Universe@Home* project⁷ and made the creation of the database used in this study possible. GW is partly supported by the President’s International Fellowship Initiative (PIFI) of the Chinese Academy of Sciences under grant no.2018PM0017 and by the Strategic Priority Research Program of the Chinese Academy of Science Multi-waveband Gravitational Wave Universe (Grant No. XDB23040000). This work is partly supported by the National Natural Science Foundation of China (Grant No. 11690024, 11873056, and 11991052) and the National Key Program for Science and Technology Research and Development (Grant No. 2016YFA0400704). SJ acknowledges funding by the European Union’s Horizon 2020 research and innovation programme from the European Research Council (ERC; Grant agreement No. 715063, PI: de Mink) and by the Netherlands Organisation for Scientific Research (NWO) as part of the Vidi research program BinWaves (project number 639.042.728, PI: de Mink). KB acknowledges support from the Polish National Science Center (NCN) grant Maestro (2018/30/A/ST9/00050).

REFERENCES

- Abbott, B. P., Abbott, R., Abbott, T. D., et al. 2016, Phys. Rev. Lett., 116, 061102
- Aitken, R. G. 1918, The binary stars
- Andrews, J. J., Breivik, K., & Chatterjee, S. 2019, arXiv e-prints, arXiv:1909.05606
- Babak, S., Gair, J., Sesana, A., et al. 2017, Phys. Rev. D, 95, 103012
- Bahcall, J. N., & Soneira, R. M. 1981, ApJS, 47, 357
- Barkat, Z., Rakavy, G., & Sack, N. 1967, Phys. Rev. Lett., 18, 379

⁷ <https://universeathome.pl/>

- Barstow, M. A., Casewell, S. L., Catalan, S., et al. 2014, arXiv e-prints, arXiv:1407.6163
- Belczynski, K., Bulik, T., Fryer, C. L., et al. 2010a, *ApJ*, 714, 1217
- Belczynski, K., Dominik, M., Bulik, T., et al. 2010b, *ApJ*, 715, L138
- Belczynski, K., Kalogera, V., & Bulik, T. 2002, *ApJ*, 572, 407
- Belczynski, K., Kalogera, V., Rasio, F. A., et al. 2008, *ApJS*, 174, 223
- Belczynski, K., Taam, R. E., Kalogera, V., Rasio, F. A., & Bulik, T. 2007, *ApJ*, 662, 504
- Belczynski, K., Hirschi, R., Kaiser, E. A., et al. 2019, arXiv e-prints, arXiv:1911.12357
- Belczynski, K., Klencki, J., Fields, C. E., et al. 2020a, *A&A*, 636, A104
- Belczynski, K., Hirschi, R., Kaiser, E. A., et al. 2020b, *ApJ*, 890, 113
- Belokurov, V., Erkal, D., Evans, N. W., Koposov, S. E., & Deason, A. J. 2018, *MNRAS*, 478, 611
- Binney, J., & Tremaine, S. 2008, *Galactic Dynamics: Second Edition*
- Bovy, J., & Rix, H.-W. 2013, *ApJ*, 779, 115
- Bray, J. C., & Eldridge, J. J. 2018, *MNRAS*, 480, 5657
- Breivik, K., Chatterjee, S., & Larson, S. L. 2017, *ApJ*, 850, L13
- Breivik, K., Coughlin, S., Zevin, M., et al. 2020, *ApJ*, 898, 71
- Bullock, J. S., & Johnston, K. V. 2005, *ApJ*, 635, 931
- Casares, J., Negueruela, I., Ribó, M., et al. 2014, *Nature*, 505, 378
- Chomiuk, L., & Povich, M. S. 2011, *AJ*, 142, 197
- de Grijs, R., & Bono, G. 2016, *ApJS*, 227, 5
- Deng, L.-C., Newberg, H. J., Liu, C., et al. 2012, *Research in Astronomy and Astrophysics*, 12, 735
- DESI Collaboration, Aghamousa, A., Aguilar, J., et al. 2016, arXiv e-prints, arXiv:1611.00036
- Di Carlo, U. N., Mapelli, M., Bouffanais, Y., et al. 2019, arXiv e-prints, arXiv:1911.01434
- Docobo, J. A., Tamazian, V. S., & Campo, P. P. 2018, *MNRAS*, 476, 2792
- El-Badry, K., & Quataert, E. 2020, *MNRAS*, 493, L22
- El Mellah, I., Sundqvist, J. O., & Keppens, R. 2019, *A&A*, 622, L3
- Eldridge, J. J. 2009, *MNRAS*, 400, L20
- Eldridge, J. J., Stanway, E. R., Breivik, K., et al. 2019, arXiv e-prints, arXiv:1912.03599
- Event Horizon Telescope Collaboration, Akiyama, K., Alberdi, A., et al. 2019, *ApJ*, 875, L1
- Fabbiano, G. 2006, *ARA&A*, 44, 323
- Farmer, R., Renzo, M., de Mink, S. E., Marchant, P., & Justham, S. 2019, *ApJ*, 887, 53
- Fox, A. J., Richter, P., Ashley, T., et al. 2019, *ApJ*, 884, 53
- Fryer, C. L., & Kusenko, A. 2006, *ApJS*, 163, 335
- Fryer, C. L., & Young, P. A. 2007, *ApJ*, 659, 1438
- Gaia Collaboration, Brown, A. G. A., Vallenari, A., et al. 2016a, *A&A*, 595, A2
- Gaia Collaboration, Prusti, T., de Bruijne, J. H. J., et al. 2016b, *A&A*, 595, A1
- Gaia Collaboration, Brown, A. G. A., Vallenari, A., et al. 2018, *A&A*, 616, A1
- Gandhi, P., Buckley, D. A. H., Charles, P., et al. 2020, arXiv e-prints, arXiv:2009.07277
- Giesers, B., Dreizler, S., Husser, T.-O., et al. 2018, *MNRAS*, 475, L15
- Gilfanov, M. 2004, *MNRAS*, 349, 146
- Gillessen, S., Eisenhauer, F., Trippe, S., et al. 2009, *ApJ*, 692, 1075
- Gould, A., & Salim, S. 2002, *ApJ*, 572, 944
- Gu, W.-M., Mu, H.-J., Fu, J.-B., et al. 2019, *ApJ*, 872, L20
- Hawking, S. W. 1974, *Nature*, 248, 30
- . 1975, *Communications in Mathematical Physics*, 43, 199
- Heger, A., & Woosley, S. E. 2002, *ApJ*, 567, 532
- Helmi, A., Babusiaux, C., Koppelman, H. H., et al. 2018, *Nature*, 563, 85
- Herant, M. 1995, *Phys. Rep.*, 256, 117
- Hobbs, G., Lorimer, D. R., Lyne, A. G., & Kramer, M. 2005, *MNRAS*, 360, 974
- Hurley, J. R., Tout, C. A., & Pols, O. R. 2002, *MNRAS*, 329, 897
- Igoshev, A. P., & Perets, H. B. 2019, *MNRAS*, 486, 4098
- Irrgang, A., Geier, S., Kreuzer, S., Pelisoli, I., & Heber, U. 2020, *A&A*, 633, L5
- Ivanova, N., & Taam, R. E. 2004, *ApJ*, 601, 1058
- Jiménez-Esteban, F. M., Torres, S., Rebassa-Mansergas, A., et al. 2018, *MNRAS*, 480, 4505
- Jordi, C., Gebran, M., Carrasco, J. M., et al. 2010, *A&A*, 523, A48
- Jurić, M., Ivezić, Ž., Brooks, A., et al. 2008, *ApJ*, 673, 864
- Karpov, S. V., & Lipunov, V. M. 2001, *Astronomy Letters*, 27, 645
- Kawanaka, N., Yamaguchi, M., Piran, T., & Bulik, T. 2017, in *IAU Symposium, Vol. 324, New Frontiers in Black Hole Astrophysics*, ed. A. Gomboc, 41–42
- Khokhlov, S. A., Miroshnichenko, A. S., Zharikov, S. V., et al. 2018, *ApJ*, 856, 158
- King, A., & Lasota, J. P. 2014, *MNRAS*, 444, L30
- Klencki, J., Nelemans, G., Istrate, A., & Pols, O. 2020, arXiv e-prints, arXiv:2004.00628
- Klencki, J., Wiktrowicz, G., Gładysz, W., & Belczynski, K. 2017, *MNRAS*, 469, 3088
- Kobayashi, C., & Nakasato, N. 2011, *ApJ*, 729, 16
- Kremer, K., Lu, W., Rodriguez, C. L., Lachat, M., & Rasio, F. A. 2019, *ApJ*, 881, 75
- Kuznetsov, A. V., & Mikheev, N. V. 2012, *Astronomy Letters*, 38, 436
- Langer, N. 2012, *ARA&A*, 50, 107
- Laplace, E., Göteborg, Y., de Mink, S. E., Justham, S., & Farmer, R. 2020, *A&A*, 637, A6
- Leung, S.-C., Nomoto, K., & Blinnikov, S. 2019, *ApJ*, 887, 72
- Licquia, T. C., & Newman, J. A. 2015, *ApJ*, 806, 96
- Liu, J., Zhang, H., Howard, A. W., et al. 2019a, *Nature*, 575, 618
- Liu, J., Zheng, Z., Soria, R., et al. 2020, arXiv e-prints, arXiv:2005.12595
- Liu, J.-F., Bregman, J. N., Bai, Y., Justham, S., & Crowther, P. 2013, *Nature*, 503, 500
- Liu, N., Fu, J.-N., Zong, W., et al. 2019b, *Research in Astronomy and Astrophysics*, 19, 075
- Lucy, L. B. 2014, *A&A*, 563, A126
- Maccarone, T. J., Kundu, A., Zepf, S. E., Piro, A. L., & Bildsten, L. 2005, *MNRAS*, 364, L61
- Makarov, V. V., & Tokovinin, A. 2019, *AJ*, 157, 136
- Mapelli, M., Spera, M., Montanari, E., et al. 2020, *ApJ*, 888, 76
- Marshall, D. J., Robin, A. C., Reylé, C., Schultheis, M., & Picaud, S. 2006, *A&A*, 453, 635
- Mashian, N., & Loeb, A. 2017, *MNRAS*, 470, 2611
- Masuda, K., & Hotokezaka, K. 2019, *ApJ*, 883, 169
- Matteucci, F., Grisoni, V., Spitoni, E., et al. 2019, *MNRAS*, 487, 5363
- Menou, K., Narayan, R., & Lasota, J.-P. 1999, *ApJ*, 513, 811
- Metzger, B. D. 2019, *Living Reviews in Relativity*, 23, 1
- Middleton, M. J., Sutton, A. D., Roberts, T. P., Jackson, F. E., & Done, C. 2012, *MNRAS*, 420, 2969
- Minniti, D., Contreras Ramos, R., Alonso-García, J., et al. 2015, *ApJ*, 810, L20
- Mohamed, S., & Podsiadlowski, P. 2012, *Baltic Astronomy*, 21, 88
- Morawski, J., Giersz, M., Askar, A., & Belczynski, K. 2018, *MNRAS*, 481, 2168
- Murray, C. D., & Dermott, S. F. 1999, *Solar system dynamics*
- Mutch, S. J., Croton, D. J., & Poole, G. B. 2011, *ApJ*, 736, 84
- Nelemans, G., Yungelson, L. R., & Portegies Zwart, S. F. 2001, *A&A*, 375, 890
- Novikov, I. D., & Zel'dovich, Y. B. 1973, *ARA&A*, 11, 387
- Olejak, A., Belczynski, K., Bulik, T., & Sobolewska, M. 2019, arXiv e-prints, arXiv:1908.08775
- Oort, J. H. 1969, *Nature*, 224, 1158
- Perets, H. B., Li, Z., Lombardi, James C., J., & Milcarek, Stephen R., J. 2016, *ApJ*, 823, 113
- Renzo, M., Farmer, R. J., Justham, S., et al. 2020, *MNRAS*, 493, 4333
- Robin, A. C., Reylé, C., Derrière, S., & Picaud, S. 2003, *A&A*, 409, 523
- Robitaille, T. P., & Whitney, B. A. 2010, *ApJ*, 710, L11
- Rodriguez, C. L., Zevin, M., Pankow, C., Kalogera, V., & Rasio, F. A. 2016, *ApJ*, 832, L2
- Romano, D., Karakas, A. I., Tosi, M., & Matteucci, F. 2010, *A&A*, 522, A32

- Ruan, W.-H., Liu, C., Guo, Z.-K., Wu, Y.-L., & Cai, R.-G. 2019, arXiv e-prints, arXiv:1909.07104
- Safarzadeh, M., Ramirez-Ruiz, E., & Belczynski, K. 2019, arXiv e-prints, arXiv:1912.10456
- Sale, S. E., Drew, J. E., Unruh, Y. C., et al. 2009, *MNRAS*, 392, 497
- Sana, H., de Mink, S. E., de Koter, A., et al. 2012, *Science*, 337, 444
- Sesar, B., Jurić, M., & Ivezić, Ž. 2011, *ApJ*, 731, 4
- Shao, Y., & Li, X.-D. 2019, arXiv e-prints, arXiv:1909.11328
- Shenar, T., Bodensteiner, J., Abdul-Masih, M., et al. 2020, arXiv e-prints, arXiv:2004.12882
- Shikauchi, M., Kumamoto, J., Tanikawa, A., & Fujii, M. S. 2020, *PASJ*, 72, 45
- Simón-Díaz, S., Maíz Apellániz, J., Lennon, D. J., et al. 2020, *A&A*, 634, L7
- Soubiran, C., & Girard, P. 2005, *A&A*, 438, 139
- Spitzer, L. 1978, *Physical processes in the interstellar medium*, doi:10.1002/9783527617722
- Takada, M., Ellis, R. S., Chiba, M., et al. 2014, *PASJ*, 66, R1
- Tetarenko, B. E., Sivakoff, G. R., Heinke, C. O., & Gladstone, J. C. 2016, *ApJS*, 222, 15
- Thompson, T. A., Kochanek, C. S., Stanek, K. Z., et al. 2019, *Science*, 366, 637
- Tomsick, J. A., & Muterspaugh, M. W. 2010, *ApJ*, 719, 958
- Toonen, S., Hamers, A., & Portegies Zwart, S. 2017, in *American Astronomical Society Meeting Abstracts*, Vol. 229, American Astronomical Society Meeting Abstracts #229, 326.05
- Torres, S., García-Berro, E., Isern, J., & Figueras, F. 2005, *MNRAS*, 360, 1381
- Trimble, V. L., & Thorne, K. S. 1969, *ApJ*, 156, 1013
- Tsuna, D., Kawanaka, N., & Totani, T. 2018, *MNRAS*, 477, 791
- van Haften, L. M., Nelemans, G., Voss, R., et al. 2013, *A&A*, 552, A69
- Vos, J., Bobrick, A., & Vuckovic, M. 2020, arXiv e-prints, arXiv:2003.05665
- Wang, H.-T., Jiang, Z., Sesana, A., et al. 2019, *Phys. Rev. D*, 100, 043003
- Wijnands, R., & van der Klis, M. 1998, *ApJ*, 507, L63
- Wiktorowicz, G., Lasota, J.-P., Middleton, M., & Belczynski, K. 2019a, *ApJ*, 875, 53
- Wiktorowicz, G., Wyrzykowski, L., Chruslinska, M., et al. 2019b, *ApJ*, 885, 1
- Woosley, S. E. 2017, *ApJ*, 836, 244
- Wyrzykowski, L., & Mandel, I. 2019, arXiv e-prints, arXiv:1904.07789
- Wyrzykowski, L., Kostrzewa-Rutkowska, Z., Skowron, J., et al. 2016, *MNRAS*, 458, 3012
- Yalinewich, A., Beniamini, P., Hotokezaka, K., & Zhu, W. 2018, *MNRAS*, 481, 930
- Yamaguchi, M. S., Kawanaka, N., Bulik, T., & Piran, T. 2018, *ApJ*, 861, 21
- Yi, T., Sun, M., & Gu, W.-M. 2019, *ApJ*, 886, 97
- Yoshii, Y. 2013, *Star Counts and Nature of the Galactic Thick Disk*, ed. T. D. Oswalt & G. Gilmore, Vol. 5, 393
- Yu, S., & Jeffery, C. S. 2015, *MNRAS*, 448, 1078
- Yungelson, L. R., Kuranov, A. G., Postnov, K. A., & Kolesnikov, D. A. 2020, *MNRAS*, arXiv:2004.11821
- Yungelson, L. R., Lasota, J. P., Nelemans, G., et al. 2006, *A&A*, 454, 559
- Zdziarski, A. A., & Gierliński, M. 2004, *Progress of Theoretical Physics Supplement*, 155, 99
- Zheng, L.-L., Gu, W.-M., Yi, T., et al. 2019, *AJ*, 158, 179
- Ziółkowski, J. 1972, *Acta Astronomica*, 22, 327
- Życki, P. T., & Niedźwiecki, A. 2005, *MNRAS*, 359, 308